Functional Genetic Screens Reveal Key Pathways Instructing the Molecular Phenotypes of Tumor-Associated Macrophages

Youxue Lu[1], Ce Luo[2], Lanxiang Huang[3], Gengyi Wu[1], Lihan Zhong[1], Jieyu Chu[1], Fubing Wang[3], Zexian Zeng[2,4,5], and Deng Pan[1,5]

ABSTRACT

Tumor-associated macrophages (TAM) display remarkable functional heterogeneity, yet the molecular mechanisms driving their diverse phenotypes remain elusive. Using CRISPR screens in primary macrophages, we identified tumor-derived factors, including lactic acid, prostaglandin E2, and GM-CSF, as key modulators of TAM polarization. These factors interacted cooperatively and antagonistically to shape distinct TAM phenotypes that were highly conserved across human cancers. Mechanistically, lactic acid and PGE2 jointly induced angiogenic gene programs while suppressing GM-CSF–driven MHC-II expression at the chromatin level, creating mutually exclusive distributions of proangiogenic and MHC-II$^+$ TAMs, which were differentially localized to specific spatial niches in the tumor microenvironment. Furthermore, we showed that shifting TAMs to an interferon-responsive phenotype, triggered by *Adar* inactivation, significantly promoted the infiltration of effector CD8$^+$ T cells through specific receptor–ligand interactions. These findings uncover a conserved mechanism of TAM polarization and offer insights into therapeutic strategies for TAM reprogramming to potentiate cancer immunotherapy.

Introduction

Tumor-associated macrophages (TAM) are highly abundant immune cells in various solid malignancies, exhibiting remarkable plasticity and adopting distinct functional phenotypes in response to local cues (1, 2). TAMs play dual roles in cancer progression—promoting angiogenesis, immune suppression, and metastasis (3) while also possessing antitumor potential through phagocytosis and immune stimulation (4, 5). Although traditionally classified as M1/M2, single-cell studies reveal a broad spectrum of TAM phenotypes (6–8), such as angiogenic TAMs marked by *SPP1*, *VCAN*, or *FN1* (7), C1QC$^+$ TAMs with inflammatory and MHC-II signatures (7, 9), interferon-stimulated gene (ISG$^+$)–positive TAMs marked by high expression of ISGs, and lipid-associated TAMs characterized by elevated lipid metabolism (6, 10).

Despite this phenotypic diversity, it remains unclear which factors within the tumor microenvironment (TME) drive the development of specific functional phenotypes in TAMs (11). To address this gap of knowledge, using an *ex vivo* tumor-educated macrophage model, we found that lactic acid and prostaglandin E2 (PGE2) coordinately induce angiogenic programs while suppressing MHC-II expression, whereas GM-CSF promotes MHC-II^{hi} TAMs. This mutual exclusivity explains their spatial distribution: angiogenic TAMs dominate hypoxic, glycolytic regions whereas MHC-II TAMs populate normoxic areas. Notably, *Adar* inactivation reprogrammed TAMs to an ISG$^+$ phenotype that enhanced CD8$^+$ T-cell activity and improved anti–PD-1 response. These results reveal conserved TAM polarization mechanisms and identify therapeutic opportunities through targeted TAM reprogramming.

Materials and Methods

Cell lines

HEK293T (RRID: CVCL_0063, received in 2020), Lewis lung carcinoma (LLC; RRID: CVCL_4358, received in 2019), 4T1 (RRID: CVCL_0125, received in 2022), Panc02 (RRID: CVCL_D627, received in 2020), MC38 (RRID: CVCL_B288, received in 2022), and B16F10 (RRID: CVCL_0159, received in 2019) cells were cultured in DMEM (Gibco, cat. #C11965500BT) supplemented with 10% FBS (ExCell Bio, cat. #FSP500), 100 μg/mL penicillin, and 100 U/mL of streptomycin (Gibco, cat. #15140122). 4T07 (RRID: CVCL_B383, received in 2020) cells were cultured in RPMI-1640 medium (Gibco, cat. #11875093) supplemented with 10% FBS, 100 μg/mL penicillin, and 100 U/mL of streptomycin. All cells were cultured at 37°C in 5% CO_2. The Panc02 cell line was purchased from Shanghai Baofeng Technology, whereas other cell lines were purchased from National Collection of Authenticated Cell Cultures. All cell lines were passaged a minimum of two times prior to experiments and avoided long passages *in vitro*. The authenticated cell lines are kept within five passages *in vitro* and have not been re-authenticated again. The cell lines were tested for *Mycoplasma* every month.

[1]School of Basic Medical Sciences, State Key Laboratory of Molecular Oncology, Tsinghua University, Beijing, China. [2]Center for Quantitative Biology, Academy for Advanced Interdisciplinary, Peking University, Beijing, China. [3]Department of Laboratory Medicine, Zhongnan Hospital of Wuhan University, Wuhan, China. [4]Peking University Chengdu Academy for Advanced Interdisciplinary Biotechnologies, Chengdu, China. [5]Tsinghua-Peking Joint Centre for Life Sciences (CLS), Beijing, China.

Y. Lu and C. Luo contributed equally to this article.

D. Pan is the lead contact.

Corresponding Authors: Fubing Wang, Department of Laboratory Medicine, Zhongnan Hospital of Wuhan University, Wuhan 430071, China. E-mail: wangfubing@znhospital.cn; Zexian Zeng, Center for Quantitative Biology, Peking University, Lv-Zhihe Building 235, Beijing 100084, China. E-mail: zexianzeng@pku.edu.cn; and Deng Pan, Department of Basic Medical Sciences, Tsinghua University, Medical Building B1005, Tsinghua University, Beijing 100084, China. E-mail: dpan@tsinghua.edu.cn

Cancer Immunol Res 2025;13:2054–74

doi: 10.1158/2326-6066.CIR-25-0488

Primary cultures

Bone marrow–derived macrophages (BMDM) were cultivated in DMEM supplemented with 20% FBS, 100 μg/mL penicillin, and 100 U/mL of streptomycin. These cultures were stimulated with 20 ng/mL of recombinant mouse macrophage (M)-CSF (Novoprotein, cat. #CP34) in 15-cm Petri dishes. Fresh medium, again supplemented with 20 ng/mL M-CSF, was then added. Fresh medium supplemented with 20 ng/mL M-CSF was replaced every 2 to 3 days and mature BMDMs were obtained after 7 days after bone marrow isolation.

Animal studies

All mice, including Rosa26-Cas9 transgenic mice (RRID: IMSR_JAX:026430), LSL-Cas9 mice (RRID: IMSR_JAX:026175), and Lyz2-Cre mice (The Jackson Laboratory) were maintained under specific pathogen-free conditions. Mice 6 to 12 weeks of age were used for all animal experiments. All animal experiments were approved by the Institutional Animal Care and Use Committee at the Tsinghua University. All mice were used in accordance with Tsinghua University Animal Ethics Committee guidelines under the protocol number 19-PD1-G22.4.

Human specimens

A total of 25 human tumor samples were collected from residual clinical tissue specimen after pathologic diagnosis. All freshly dissected tumor samples were kept on ice and processed to next steps for FACS analysis or spatial omics immediately. The usage of these samples was permitted with informed consent approved by the Medical Ethics Committee of Zhongnan Hospital at Wuhan University (2023073K) and was in accordance with the Declaration of Helsinki. Peripheral blood mononuclear cells of healthy donors were purchased from Milestone Biotechnologies (cat. #PB010C). All human participants provided written informed consent prior to their participation in the study. There were no specific exclusion criteria for the tumor samples obtained for analysis.

Flow cytometric analysis of human TAMs

Fresh surgical resection specimens were collected from patients with lung, breast, and colorectal cancer. Tumor tissues were excised and digested with collagenase IV (Sigma, cat. # C5138), DNase I (Sigma, cat. # D5025), and hyaluronidase (Sigma, cat. #H6254) in 5 mL of RPMI-1640 (Gibco) in C-tubes (Miltenyi Biotec) and incubated at 37°C for 30 minutes, followed by processing via GentleMACS. Single-cell suspension was obtained by filtering the cells through a 70-μm cell strainer. Cells were first stained with the Zombie-NIR Fixable Viability Kit (BioLegend, cat. #423106) in PBS and then stained with Human TruStain FcX (BioLegend, cat. #422302, RRID: AB_ 2818986) to block the IgG Fc receptor. The cells were stained with surface markers of anti-CD45 (BioLegend, cat. #368522, RRID: AB_2687375), anti-CD11b (BioLegend, cat. #301334, RRID: AB_2562112), and anti-HLA-DR, -DP, and -DQ (BioLegend, cat. #361714, RRID: AB_2750316) antibodies, fixed, and permeabilized for intracellular staining of anti-VEGFA (Proteintech, cat. #CL594-66828, RRID: AB_3084729) and anti-CD68 (BioLegend, cat. #333806, RRID: AB_1089054) antibodies.

Integrative analysis and re-annotation of single-cell transcriptional atlas of human TAMs

Data for the single-cell transcriptional atlas of tumor-infiltrating myeloid cells were obtained from the referenced study (7). Specifically, we extracted all macrophage cells originating from tumor samples, encompassing 35,282 cells across 108 samples from 15 cancer types. Based on the annotation provided in the referenced study (7), all cells classified as macrophages (including subclusters such as Macro_C1QC, Macro_ISG15, Macro_PPARG, Macro_SPP1, and others) were selected for downstream analysis. These macrophages were re-integrated using single-cell variational inference (RRID: SCR_026673) across cancer types following the "atlas-level integration tutorial" (https://docs.scvi-tools.org/en/stable/tutorials/notebooks/scrna/harmonization.html).

In selecting the gene lists for macrophage phenotype analysis, we relied on well-established literature, primarily from Ma and colleagues (12), Trends in Immunology, 2022. These selections were based on their widespread recognition and validation within the scientific community. Additionally, our list was validated through cross-referencing multiple studies, ensuring a robust and accurate representation of the targeted phenotypes. We curated four major human TAM signatures, including MHC-II$^+$ TAMs, ISG$^+$ TAMs, lipid-associated TAMs, and angiogenic TAMs (see Supplementary Table S1). Using the decoupler.run_aucell() function from the decoupler Python package (RRID: SCR_008394), we applied the AUCELL algorithm (RRID: SCR_021327) to infer the biological activities of the four programs within each macrophage. Subsequently, pairwise Pearson correlation coefficients were computed for the scores.

We re-annotated the pan-cancer TAMs into five categories: MHC-II$^+$ TAMs, ISG$^+$ TAMs, lipid-associated TAMs, angiogenic TAMs, and undetermined. The workflow is as follows:

(1) The distribution of the maximum score [denoted as $\max(score_i)$] for each cell across the dataset had a mean (μ) of 0.473 and an SD (σ) of 0.126. The threshold for the maximum score was set at μ − 2*σ (0.221), rounded to 0.2 for simplicity.
(2) The proportion of each signature score relative to the total sum of all four scores for a given cell was calculated:

$$score_i\ ratio = \frac{score_i}{\sum_{j=1}^{4} score_j}$$

(3) The distribution of the maximum proportion values [denoted as $\max(score_i\ ratio)$] for each cell across the dataset had a mean (μ) of 0.49 and an SD (σ) of 0.098. The threshold for the maximum proportion was set at μ − σ (0.392), rounded to 0.4 for simplicity.
(4) The difference (Δ) is defined as the subtraction of the second-highest score proportion [denoted as $second(score_i\ ratio)$] from the maximum score proportion.

$$\Delta = \max(score_i\ ratio) - second(score_i\ ratio)$$

The distribution of the difference (Δ) had a mean (μ) of 0.23 and an SD (σ) of 0.14. The threshold for this difference (Δ) was set at σ (0.14), rounded to 0.1 for simplicity.

Macrophage cells were annotated using the following criteria:

(1) Cells with a maximum score value [$\max(score_i)$] less than 0.2 were labeled as undetermined, resulting in a total of 679 cells.
(2) For the remaining cells, those with $\max(score_i\ ratio) > 0.4$ and $\Delta > 0.1$ were annotated according to the signature corresponding to the maximum score proportion.
(3) The remaining cells from step (1) that did not meet the criteria in step (2) were also labeled as undetermined.

Survival analysis in The Cancer Genome Atlas cohorts

Transcriptomic [RNA sequencing (RNA-seq) gene expression] and clinical data were retrieved from The Cancer Genome Atlas

(TCGA) Data Portal (https://www.cancer.gov/tcga) for three cancer types: TCGA-LUAD (lung adenocarcinoma, $n = 464$), TCGA-CESC (cervical squamous cell carcinoma and endocervical adenocarcinoma, $n = 276$), and TCGA-SKCM (skin cutaneous melanoma, $n = 97$). Clinical information included overall survival (OS) and survival status, in which OS was defined as the time interval from the date of diagnosis to either the date of death or the last follow-up. Patients were stratified into high versus low groups according to their angiogenesis (Angio.SIG) or MHC-II (MHC-II.SIG) signature scores using the median as the cutoff. Kaplan–Meier survival analysis was performed to estimate OS using the Python package lifelines v0.21.0 (RRID: SCR_024899). Group differences were assessed using the log-rank test, with corresponding *P* values reported.

Tumor-educated macrophages related experiments

Generation of tumor-educated macrophages

Bone marrow cells were isolated and then treated with 20 ng/mL of recombinant mouse M-CSF for 6 days to generate BMDMs. On day 6, BMDMs were cultured in a 1:1 mixture of fresh media and tumor-conditioned media (TCM) for another 4 days in the presence of M-CSF to generate tumor-educated macrophages (TEM). For TCM harvest, tumor cells were seeded at approximately 20% confluency and then cultivated for 48 hours without replacing the media. TCM was collected and filtered (0.22 μm) at 48 hours when confluency reached more than 90%.

CRISPR-mediated knockout in TEMs

(1) Constructing a single-guide RNA (sgRNA)–expressing vector that is highly efficient in primary macrophages:

The backbone retroviral vector pMYs-GFP (Cell Biomabs, RTV-052) was obtained from Dr. Mo Chen's lab at Tsinghua University. We then generated the pMYs-GFP-U6-BbsI vector, which enables us to clone sgRNA efficiently. For sgRNA cloning, annealed oligos can be directly inserted into BbsI-linearized pMYs-GFP-U6-BbsI by T4 ligation similar to the cloning method of lentiCRISPR v2. sgRNAs were designed and picked by using CRISPick software (https://portals.broadinstitute.org/gppx/crispick/public).

(2) Infection of BMDMs with retrovirus:

HEK293T cells were seeded in a six-well plate at a density of 0.8×10^6 cells per 2 mL DMEM supplemented with 10% FBS and 1% penicillin/streptomycin. A day later, cells in each well were transfected with 1.5 μg of the targeting vector pMYs-GFP-U6-sgRNA and 1.5 μg of the packaging vector pCL-Eco (RRID: Addgene_12371), using 12 μL of 1 mg/mL PEI max (Polysciences, cat. #24765), following a standard protocol. The retroviral supernatant was collected at 48 and 72 hours after transfection.

The template insert sequences for the U6 promoter and sgRNA are as follows (sgRNA scaffold underlined):

GAGGGCCTATTTCCCATGATTCCTTCATATTTGCATATACGATACAAGGCTGTTAGAGAGATAATTGGAATTAATTTGACTGTAAACACAAAGATATTAGTACAAAATACGTGACGTAGAAAGTAATAATTTCTTGGGTAGTTTGCAGTTTTAAAATTATGTTTTAAAATGGACTATCATATGCTTACCGTAACTTGAAAGTATTTCGATTTCTTGGCTTTATATATCTTGTGGAAAGGACGAAACACCGGGTCTTCGAGAAGACCTGTTTTAGAGCTAGAAATAGCAAGTTAAAATAAGGCTAGTCCGTTATCAACTTGAAAAAGTGGCACCGAGTCGGTGC

BMDMs from Cas9-expressing mice were freshly isolated and transduced by replacing 50% of the BMDM medium with the retroviral supernatant, supplemented with M-CSF for differentiation. Fresh medium supplemented with M-CSF was replaced every 2 to 3 days, and mature BMDMs were obtained on the seventh day after bone marrow isolation. TEMs were then generated by treating these BMDMs with TCM. The sequences of retroviral sgRNA inserts are listed in Supplementary Table S2.

T-cell suppression assay using TEMs

Carboxyfluorescein diacetate succinimidyl ester (BD Biosciences, cat. #565082)–labeled splenocytes from wild-type B6 mice were isolated and activated by anti–mouse CD3 (Bio X Cell, cat. #BE0001-1, RRID: AB_1107634)/CD28 (Bio X Cell, cat. #BE0015-1, RRID: AB_1107624) antibodies for 24 hours and then cocultured with TEMs in the presence of 30 IU/mL recombinant mouse IL2 (PeproTech, cat. #212-12-20UG) for 72 hours. Cell proliferation indicated by carboxyfluorescein diacetate succinimidyl ester staining was determined by flow cytometry. Beckman CytoFLEX S was used for FACS data collection and FlowJo v10.8.1 (RRID: SCR_008520) was used for data analysis.

Treatment of BMDMs with GM-CSF, lactic acid, and PGE2

BMDMs were generated by treating bone marrow–isolated cells with 20 ng/mL of recombinant mouse M-CSF as described in the "Generation of tumor-educated macrophages" section. These cells were then treated with either 2 ng/mL GM-CSF (PeproTech, cat. #315-03-20 μg), 100 nmol/L of PGE2 (Sigma, cat. #P0409-1MG), 25 mmol/L of lactic acid (Sigma, cat. #L6402-1G), or combinations of these factors. BMDMs treated with PBS (Solarbio, cat. #P1020) and DMSO (Sigma, cat. #D2650) were used as vehicle control in this experiment. These cells were then harvested and analyzed for the expression of ARG1 by FACS and transcriptome by RNA-seq.

Assay for transposase-accessible chromatin using sequencing of BMDMs treated with GM-CSF, lactic acid, and PGE2

BMDMs were treated with single or combinational treatment of GM-CSF, lactic acid, and PGE2 as described in the "Treatment of BMDMs with GM-CSF, lactic acid, and PGE2" section. Cells were harvested and 1×10^5 cells were collected in triplicates for each group. Assay for transposase-accessible chromatin using sequencing (ATAC-seq) was performed using the TruePrep DNA Library Prep Kit V2 for Illumina (Vazyme, cat. #TD501) as per the manufacturer's instructions. Cells were lysed in 50 μL lysis buffer (10 mmol/L Tris-HCl (pH 7.4), 10 mmol/L NaCl, 3 mmol/L MgCl2, and 0.5% NP-40) on ice for 10 minutes. Nuclei were isolated by centrifugation at $500 \times g$ for 10 minutes and then resuspended in 50 μL of transposition mix (10 μL 5 × TTBL, 5 μL TTE Mix V50, and 35 μL ddH2O) at 55°C for 10 minutes. DNA was purified by VAHTS DNA Clean Beads (Vazyme, cat. #N411) and ligated with adapters and amplified to a target concentration. Libraries were size selected using VAHTS DNA Clean Beads (Vazyme, cat. #N411) and sequenced.

Treatment of human primary macrophages with GM-CSF, lactic acid, and PGE2

$CD14^+$ monocytes were isolated from peripheral blood mononuclear cells using anti-CD14 magnetic beads (Miltenyi Biotec, cat. #130-050-201) and cultured in above 90%, measured by flow cytometry. Monocytes were seeded (1×10^6/mL) in 24-well plates and cultured in Iscove's Modified Dulbecco's Medium (Gibco, cat. #12440053) supplemented with 10% FBS, 1%

penicillin/streptomycin, 2 mmol/L glutamine (Gibco, cat. #35050061), and 2β-mercaptoethanol (50 μg/mL, Gibco, cat. #21985023) containing human recombinant M-CSF (10 ng/mL; PeproTech, cat. #300-25). These cells were then treated with 2 ng/mL GM-CSF or 25 mmol/L lactic acid and 100 nmol/L PGE2 for 24 hours. Cells treated with PBS and DMSO were used as vehicle control in this experiment. These cells were then harvested and analyzed for the expression of HLA-DR, -DP, and -DQ by FACS and transcriptome by RNA-seq.

In vitro CRISPR screen to identify regulators of angiogenic TEMs

Library design and cloning

For screening in primary macrophages, we created a library of 10,200 optimized sgRNAs targeting 2,245 genes (Supplementary Table S8) that were expressed in both murine and human macrophages. These genes were selected from the following Gene Ontology term categories: kinase, phosphatase, cell surface, plasma membrane, antigen processing and presentation, immune system process, metabolism, and chromatin remodeling. To create a pooled sgRNA library in pMYs-GFP-U6-BbsI, oligo pool was amplified via NEBNext Ultra II Q5 Master Mix (NEB, cat. #M0544L) and cloned into vector by T7 ligase (NEB, cat. #M0318L).

CRISPR screen in TEMs

Bone marrow cells were first isolated from the Cas9 transgenic mice and were then infected with sgRNA retroviral library with multiplicity of infection<0.3 in the presence of 20 ng/mL of recombinant mouse M-CSF. On day 3, medium was replaced with fresh medium supplemented with 20 ng/mL M-CSF. On day 5, GFP-positive BMDMs were sorted and seeded at 5×10^6 cells per 15-cm Petri dish. On day 6 and day 8, 50% of BMDM medium was replaced with 4T1-TCM to generate TEMs. On day 10, approximately 5×10^6 GFP-positive cells were harvested and intracellular staining was performed for ARG1. ARG1-negative TEMs were then sorted by FACS for genomic DNA extraction by using the NucleoSpin Tissue kit (MACHEREY-NAGEL) according the manufacturer's protocol. Amplification of the sgRNA by PCR and next-generation sequencing was performed according to the broad GPP protocol (https://portals.broadinstitute.org/gpp/public/resources/protocols).

MAGeCK (13) v0.5.9.2 software was used to process and analyze the CRISPR screen data. Sequence reads were trimmed and mapped to the library using the MAGeCK "count" function to calculate sgRNA read counts. Quality control was performed on both FASTQ and count files. The MAGeCK "test" module was used to identify gene targets with significantly enriched or depleted sgRNA in the non-angiogenic group ($ARG1^-$) compared with the input control. The "–control-sgrna" parameter was used to specify the control sgRNAs, and "–norm-method control" was used to normalize the data using these controls. MAGeCK provided sgRNA and gene FDR and $\log_2$ fold change statistics, indicating the enrichment levels of sgRNAs and genes.

Target validation in TEMs

Bone marrow cells isolated from Cas9 mice were transduced with sgRNAs of interest and then were induced into TEMs (as described in detail in previous section "CRISPR-mediated knockout in TEMs"). The sequences of sgRNA for validation experiments were listed in Supplementary Table S2. Transduced TEMs were harvested and fixed with 4% paraformaldehyde, followed by two washes of diluted permeabilization buffer (Invitrogen, cat. #88-8824-00). The cells were first treated with anti–mouse CD16/CD32 (BioLegend, cat. #101320, RRID: AB_1574975) to block Fc receptor and were then stained with antibodies against ARG1 (Thermo Fisher Scientific, cat. #17-3697-82, RRID: AB_2734835). GFP^+ transduced cells were gated for ARG1 quantification in TEMs expressing specific sgRNA.

Quantification of lactic acid, PGE2, and GM-CSF in tumor knockout cell lines

Generation of *Csf2* and *Cox2* knockout 4T1 cells

To inhibit PGE2 and GM-CSF expression in tumor cells, sgRNAs targeting *Cox2* and *Csf2* were cloned into the lentiCRISPR v2 (RRID: Addgene_52961) vector as standard protocol. sgRNA constructs were co-transfected with psPAX2 (RRID: Addgene_12260) and pMD2.G (RRID: Addgene_12259) and mixed with 1:3 PEI max in Opti-MEM for lentivirus production. 4T1 cells were transduced with lentivirus expressing sgRNAs. After puromycin selection, knockout (KO) cells were expanded and obtained for TCM collection.

ELISA quantification of PGE2 and GM-CSF for *in vitro* assay

To quantify PGE2 and GM-CSF release, 1.6×10^6 control and KO 4T1 cells were inoculated in 10-cm cell culture dish and TCM was harvested after 2 days' culture and filtered using a 0.22-μm filter to remove debris. GM-CSF (Mouse GM-CSF ELISA kit, Proteintech, cat. #KE10015) or PGE2 (Prostaglandin E2 Express ELISA Kit, Cayman Chemical, cat. #5100141) was measured following the manufacturer's instructions. Absorbance was measured on a BioTek Epoch2 Microplate Spectrophotometer.

Steady-state metabolite analysis of lactic acid and PGE2 for *in vivo* assay

To confirm the KO efficacy of *Ldha*/*Cox2*-KO cells, 4×10^5 control and KO 4T1 cells were inoculated in a six-well plate and TCM was harvested after 2 days' culture and filtered using a 0.22-μm filter to remove debris. With 1.2 mL of methanol, 300 μL of the filtered supernatant was mixed (Fisher chemical, cat. #A452-4) and incubated overnight at −80°C. Following a similar centrifugation and supernatant transfer procedure, samples were dried in a SpeedVac and stored at −80°C until LC/MS analysis. These experiments were conducted in triplicates. Data normalization employed MinMax normalization across all measured metabolites in each sample. The abundance of each metabolite was then calculated relative to the control sample.

Experiments and analysis related to *in vitro* treatment of lactic acid, PGE2, and GM-CSF in macrophages

Bulk RNA-seq sample preparation and analysis

BMDMs were treated with single or combinational treatment of GM-CSF, lactic acid, and PGE2 as described in the "Treatment of BMDMs with GM-CSF, lactic acid, and PGE2" section. RNA from 5×10^5 cells was extracted and purified with TRIzol reagent (Invitrogen, cat. #15596018CN) according to the manufacturer's instructions. RNA-seq libraries were prepared using the TruSeq Stranded mRNA kit (Illumina, cat. #20020594) following the manufacturer's instructions with 5 μg of input RNA, and data were collected by paired-end sequencing. To enable consistent analysis of bulk RNA-seq data, we employed the RNA-seq immune analysis pipeline (14). Sequencing reads were aligned to the mouse reference genome (GRCm38/mm10) using STAR (RRID: SCR_004463)

v2.6.1d. Transcripts were mapped to genes and a gene count matrix was generated with Salmon (RRID: SCR_017036) v0.13.1. Differentially expressed genes (DEG) were determined using DESeq2 (RRID: SCR_015687) v1.34.0, applying a significance threshold of adjusted *P* value (FDR) < 0.05. Replicates for each condition were included as a covariate in the DESeq2 analysis. For pre-ranked gene set enrichment analysis (GSEA; RRID: SCR_003199), significant differential genes (FDR<0.05) were ranked using the $\log_2$ fold change (LFC) derived from the differential expression analysis result. Pre-ranked GSEA was performed using the mouse Hallmark collections in the Molecular Signatures Database (MSigDB) (RRID: SCR_016863).

Pathway enrichment analysis

Overrepresentation enrichment analysis was conducted for gene lists using the Python package GSEApy (RRID: SCR_025803) v1.1.2. DEGs were filtered by removing pseudogenes (those starting with "Gm" or containing "-ps"). Genes with adjusted *P* value (FDR) < 0.05 were then sorted by LFC. The top 200 downregulated genes (LFC < 0) were selected. Enrichment analysis was performed using the mouse hallmark gene sets from MSigDB (RRID: SCR_016863) with the function gseapy.enrichr().

Correlation analysis of differential gene expression across BMDMs treated with TCM or tumor-derived factors

DEGs were identified for each group of BMDMs treated with 4T1-TCM or specified tumor-derived factors compared with the vehicle control BMDMs, using criteria of FDR < 0.05 and LFC > 1. The LFC values of these DEGs were then used to calculate Pearson correlation coefficients between each pair of BMDM groups. These correlation coefficients were visualized in the heatmap to illustrate the similarity in gene expression changes across the experimental conditions.

Analysis of GM-CSF–, lactic acid–, and PGE2-induced gene signatures in TAM subsets

Differential expression results for each single factor or combination of factors were compared with untreated control using DESeq2 as previously described. The results were filtered to exclude pseudogenes (genes with prefixes "Gm" or containing "-ps" or "-rs"). Only genes detected in the CRISPR droplet sequencing (CROP-seq) dataset were retained. DEGs were identified with a baseMean > 200 and an FDR < 0.05. DEGs were sorted in descending order by LFC. The top 50 upregulated genes (LFC >0) for each condition were defined as corresponding factor-induced signature. The human homologs of these signatures were stored as human signature counterparts (see Supplementary Table S3).

Low-input RNA-seq and ATAC-seq of TAMs isolated from mouse models

Tumor tissues were processed into single cells as described in the previous section "Flow cytometric analysis of human TAMs". Cells are stained with surface markers, followed by CD16/32 blocker. 4′,6-diamidino-2-phenylindole (DAPI) was added to distinguish live and dead cells. Monocytes/neutrophils ($DAPI^-CD45^+CD11b^+Ly6C/G^+$), angiogenic TAMs ($DAPI^-CD45^+CD11b^+Ly6C/G^-CX3CR1^-MHC\text{-}II^-$), and MHC-II$^+$ TAMs ($DAP^-CD45^+CD11b^+Ly6C/G^-CX3CR1^+MHC\text{-}II^+$) were sorted for library construction. For ATAC-seq and low-input RNA-seq, 2 to 5 × 10^4 cells per replicates were used.

ATAC-seq

ATAC-seq of TAMs was performed using the Hyperactive ATAC-Seq Library Prep Kit for Illumina (Vazyme, cat. #TD711). In triplicates per group, 2 to 5 × 10^4 cells were sorted and washed first with cold 1× PBS and then with TW buffer. Cells were lysed in 50 μL of RS buffer supplemented with 0.1% NP-40, 0.01% digitonin, and 0.1% Tween 20 for 5 minutes on ice. Nuclei were isolated by centrifugation at 500 × *g* for 10 minutes and then resuspended in 50 mL of transposition mix (16.5 μL TW buffer, 10 μL 5× TTBL, 4 μL TTE Mix V50, 0.5 μL 1% digitonin, 0.5 μL 10% Tween 20, and 18.5 μL ddH2O) at 37°C for 30 minutes. DNA was purified by VAHTS DNA Clean Beads (Vazyme, cat. #N411) and ligated with adapters and amplified to a target concentration. Libraries were size selected using VAHTS DNA Clean Beads (Vazyme, cat. #N411) and sequenced.

For ATAC-seq analysis, the ENCODE ATAC-seq pipeline v2.2.2 (https://github.com/ENCODE-DCC/atac-seq-pipeline) was used for quality control and preprocessing of the ATAC-seq FASTQ files, aligning them to the mm10 genome and generating BAM files. Genrich with ATAC-seq mode (https://github.com/jsh58/Genrich) was used as the peak caller with a *P* value threshold of 0.01. Additionally, Genrich was used to call peaks for replicates within the same group using the joint replicate peak calling mode.

After merging replicates, ATAC-seq peaks from different groups were combined using "bedtools merge" to create a union set of sites. The "bedtools intersect" tool (RRID: SCR_006646) was employed to identify common or group-specific peaks. BAM files were converted to bigWig files using "bamCoverage". The bigWig files from different replicates were merged using USCS Genome Browser tools "bigWigMerge" and "bedGraphToBigWig" (RRID: SCR_007708). DeepTools was used to generate heatmap plots (RRID: SCR_016366).

Differential peaks between treatment and control groups were identified using the DiffBind package (RRID: SCR_012918) with an FDR<0.05 and |Fold| > 0. Coverage files were visualized using the Integrative Genomics Viewer (RRID: SCR_011793) . For motif enrichment analysis, the HOMER findMotifsGenome.pl utility (RRID: SCR_010881) was used to screen for enrichment of known motifs in the indicated peak set relative to a background peak set.

Low-input RNA-seq

RNA from 2 to 5 × 10^4 cells was extracted by TCL buffer (Qiagen, cat. #1070498) and RNA Clean beads (Vazyme, cat. #N412) and reverse transcribed using Maxima H Minus Reverse Transcriptase (Thermo Fisher Scientific, cat. #EP0751) to generate high-quality full-length cDNA. cDNA was amplified by 2× KAPA PCR mix (TOYOBO, cat. #KK-2602) and 10 ng amplified cDNA was modified into sequencing-competent libraries using the TruePrep DNA Library Prep Kit V2 for Illumina (Vazyme, cat. #TD501) as per the manufacturer's instructions. For functional enrichment analysis, the hypergeometric overlap statistic tool (http://software.broadinstitute.org/gsea/msigdb/annotate.jsp) was used to calculate the overlap between a gene list and pathways in MSigDB. Top 200 upregulated genes (FDR < 0.05) of each group were applied for enrichment analysis using the mouse Hallmark collections in the MSigDB database.

In vivo CROP-seq experiments

Hematopoietic stem cell isolation, culture, and lentiviral transduction

The culture and expansion of hematopoietic stem cells (HSC) were performed according to a protocol described previously (15, 16). Femurs and tibias were isolated from CD45.2$^+$*Lyz2-Cre, LSL-Cas9* donor mice, crushed, and ACK-lysed. c-Kit$^+$ HSCs were isolated via magnetic selection by anti–mouse CD117 beads (Miltenyi Biotec, cat. #130-091-224) and then plated onto a 10 μg/mL fibronectin (Sigma, cat. #F0895)-coated 96-well plate and cultured in

HSC complete medium supplemented with 100 ng/mL murine thrombopoietin (TPO; Novoprotein, cat. #CP40) and 10 ng/mL murine stem cell factor (SCF; PeproTech, cat. #250-03). Between day 5 and 7 after isolation, HSCs were spin-transduced with polyethylene glycol 8000–concentrated lentivirus on retronectin (15 μg/mL; Takara, cat. #T100A)-coated 96-well plates. After 48 hours of lentiviral infection, the HSCs were transferred back to a fibronectin-coated 96-well plate for further expansion. After 4 to 7 days, GFP^+ HSCs were sorted and allowed to expand for an additional 2 weeks. These expanded HSCs were again checked for their stem cell status by staining with CD117 and were subsequently used for bone marrow transplantation. The sgRNAs included for *in vivo* CROP-seq are listed in Supplementary Tables S4 and S5.

Adoptive transfer of HSCs

$CD45.1^+$ recipient B6 mice were lethally irradiated with two 5.5 Gy doses separated by 3 hours. Irradiated mice were adoptively transferred with 1×10^6 of above-mentioned expanded HSCs from $CD45.2^+$ mice (*LSL-Cas9;Lyz2-Cre*) on the same day of irradiation. Mice were maintained on 1 mg/mL neomycin and 0.1 mg/mL polymyxin B antibiotics diluted in drinking water for 3 to 4 weeks after reconstitution. Mice were injected with tumor cells 6 to 8 weeks after HSC transfer.

In vivo CROP-seq

HSCs with myeloid-specific Cas9 were transduced with an sgRNA library at a multiplicity of infection of less than 0.3. Transduced HSCs were then expanded and transferred into lethally irradiated $CD45.1^+$ recipient mice ($n = 3$) as described above. After 6 weeks, 1.5×10^6 LLC tumor cells were subcutaneously injected into the flank of the recipient mice. The mice were sacrificed on day 14 after tumor inoculation, and TAMs derived from the transferred HSCs ($DAPI^-CD45.2^+CD11b^+Ly6C/G^-GFP^+$) were sorted using FACS. These sorted cells were pooled for CROP-seq. Single-cell suspensions (2×10^5 cells/mL) with PBS (HyClone) were loaded onto a microwell chip using the Singleron Matrix Single Cell Processing System. Barcoding Beads were subsequently collected from the microwell chip, followed by reverse transcription of the mRNA captured by the Barcoding Beads and to obtain cDNA and PCR amplification. The amplified cDNA was then fragmented and ligated with sequencing adapters. The single-cell RNA-seq (scRNA-seq) libraries were constructed according to the protocol of the GEXSCOPE Single Cell RNA Library Kits (Singleron; ref. 17). Individual libraries were diluted to 4 nmol/L, pooled, and sequenced on Illumina NovaSeq 6000 with 150 bp paired-end reads. For sgRNA amplification, three rounds of PCR were performed using the following primers (5′-3′): first round of PCR: forward-TCCCTACACGACGCTCTTCCGATCT; reverse-GGACTATCATATGCTTAC CGTAAC, second round of PCR: forward-AATGATACGGCGACCACCGAGATCTACAC TCTTTCCCTACACGACGCTCTTCC; reverse-ACTGGAGTTCAGA CGTGTGCTCTT CCGATCTTATCTTGTGGAAAGGACGAAACA-C, and third round of PCR: forward-AATGA TACGGCGACCAC-CGAGATCT, reverse-CAAGCAGAAGACGGCATACGAGATTCG CCTTAGTGACTGGAGTTCAGACGTGTGCTCTT.

CROP-seq data processing and analysis

FASTQ file processing

Raw reads from scRNA-seq were processed to generate gene expression matrixes using the CeleScope (https://github.com/singleron-RD/CeleScope) v1.11.1 pipeline. Briefly, raw reads were first processed with CeleScope to remove low-quality reads with Cutadapt (RRID: SCR_011841) v3.7 to trim poly-A tail and adapter sequences. Cell barcode and unique molecular identifier (UMI) were extracted. After that, we used STAR v2.6.1b to map reads to the reference genome GRCm39. UMI counts and gene counts of each cell were acquired with featureCounts (RRID: SCR_012919) v2.0.1 and used to generate expression matrix files for subsequent analysis.

sgRNA assignment

To assign sgRNAs to corresponding cell barcodes, we used the multi_tag module of CeleScope. This module enabled us to demultiplex and quantify sgRNA sequences in each cell. In brief, it first checks the mismatches between linker sequences (we set it as the constant 25/26 nt sequences before sgRNA sequence). If mismatch ≥ len(linker)/10 + 1, the read is classified as "invalid". Next, we determined the minimum sgRNA UMI threshold, denoted as UMI_min. UMI_min is calculated as the min (the fifth percentile of sgRNA UMI counts of all cells, one tenth of the median of sgRNA UMI counts across all cells). If the calculated value is less than 1, UMI_min is set to 1. Cells with valid sgRNA UMIs below this threshold are classified as "undetermined". Simultaneously, the method calculates the minimum signal-to-noise ratio (SNR_min) for each cell barcode. SNR is computed as the ratio of the signal (the highest sgRNA UMI count) to the noise (the second highest sgRNA UMI count). If the noise is zero, the SNR is defined as infinity. Cell barcodes with sgRNA UMIs ≥ UMI_min and with an SNR < SNR_min are classified as "multiplets". Cell barcodes passed above thresholds were assigned a guide with the highest sgRNA UMI count. To ensure the accuracy of sgRNA sequences, we modified the source code in the multi_tag module of CeleScope and set the n_mismatch parameter to 0. This alteration ensures that no mismatches are allowed in the sgRNA sequences. The guide assignments were added to the Scanpy annotation of observations for downstream processing.

Single-cell clustering and visualization

Scanpy (RRID: SCR_018139) v1.9.3 was used for quality control, dimensionality reduction, and clustering. All data were processed using the Scanpy standard analysis workflow (https://www.sc-best-practices.org/preamble.html), and clusters of each dataset were annotated according to the marker genes. In the *in vivo* CROP-seq data, initial clusters with fewer than 100 cells were eliminated, and re-clustering was performed to refine the clusterings. The *in vivo* CROP-seq data were from two batches, the *in vivo* hit validation pool (Supplementary Table S4) and the LGP validation pool (Supplementary Table S5). The algorithm Harmony (RRID: SCR_022206) was used for batch effect removal and integration. The cluster-specific or gene knockout–specific marker genes were identified by using the scanpy.tl.rank_genes_groups() function with default parameters. Six TAM signatures were analyzed in CROP-seq data, including four classical signatures ($MHCII^+$ TAMs, ISG^+ TAMs, lipid-associated TAMs, and angiogenic TAMs) and two additional signatures activated by specific gene perturbation (oxidative phosphorylation TAMs and TAMs in cell cycle; see Supplementary Table S6).

Hypoxia detection in mouse models

For assessment of tumor hypoxia, pimonidazole (60 mg/kg of body weight) was intraperitoneally injected 60 minutes prior to euthanasia.

Flow cytometric analysis

Tumor tissues were processed into single cells as described in previous section "Flow cytometric analysis of human TAMs". Cells were first stained with the Zombie-NIR Fixable Viability Kit (BioLegend, cat. #423106) in PBS and then stained with anti-mouse CD16/32 (BioLegend, cat. #101320, RRID: AB_1574975) to block the IgG Fc receptor. The cells were stained with surface markers [BV421 anti-CD45 (BioLegend, cat. #103133, RRID: AB_10899570), PerCP-Cy5.5 anti-CD11b (BioLegend, cat. #101227, RRID: AB_893233), BV510 anti-Ly6C/G (BioLegend, cat. #108438, RRID: AB_2562215), APC anti-CX3CR (BioLegend, cat. #149007, RRID: AB_2564491), and FITC anti-MHC-II (BioLegend, cat. #107606, RRID: AB_313321)], fixed using the intracellular staining kit (eBioscience, cat. #88-8824-00), and permeabilized for intracellular staining of Dylight 549 anti-pimonidazole (Hypoxyprobe, cat. #HP-7). Beckman CytoFLEX S was used for FACS data collection and FlowJo v10.8.1 (RRID: SCR_008520) was used for data analysis.

Immunofluorescence

Tumors were harvested and fixed in 20% sucrose + 4% paraformaldehyde solution in PBS overnight at 4°C. They were then embedded in optimal cutting temperature (OCT) compound (Fisher Health Care, cat. #23-730-571) and stored in −80°C. OCT blocks were cut into 10-μm sections and adhered to glass slides. The slides were stained with anti-F4/80 (Cell Signaling Technology, cat. #30325, RRID: AB_2798990), anti-pimonidazole (Hypoxyprobe, cat. #HP3-100Kit, RRID: AB_2934099), and anti-CD74 (Abcam, cat. #ab289885) using tyramide signal amplification technology. The slides were then incubated with DAPI and washed with PBS. Slides were scanned using a Pannoramic MIDI (3DHISTECH) automatic digital slide scanner, visualized using CaseViewer2.4, and analyzed using Image-Pro 641 Plus 6.0 (RRID: SCR_007369).

Spatial resolved transcriptomics and metabolomics experiments

Visium CytAssist v2 spatial transcriptomics for fresh frozen tissue

Two freshly collected human lung cancer tissue samples were divided into appropriate size and embedded in OCT and quickly frozen on dry ice. Tissue sections were subjected to methanol fixation, hematoxylin and eosin (H&E) staining, imaging, and destaining following the 10x Genomics recommended experimental procedure (CG000614). According to the 10x Genomics experimental flow (CG000495), probe hybridization and probe release were performed and transferred to the 10x Visium CytAssist slide, and the library construction was performed using the Visium CytAssist Spatial Gene Expression for FFPE kit (PN-1000520 for human, 6.5 mm). The DNA libraries were subjected to high-throughput sequencing using the PE-150 mode.

Ambient air flow–assisted desorption electrospray ionization-mass spectrometry imaging spatial metabolomics for fresh frozen tissue

MS-grade acetonitrile (ACN) was purchased from Thermo Fisher Scientific. Purified water was obtained from Watsons. Formic acid was provided by Merck, the tissue freezing medium was obtained from Leica (Leica Microsystem), eosin Y-solution 0.5% aqueous, and hematoxylin was purchased from Sigma-Aldrich. The embedded samples were stored at −80°C before being sectioned. The samples were cut into consecutive sagittal slices of 10 μm about 10 slices by a cryostat microtome (Leica CM 1950, Leica Microsystem) and were thaw-mounted on positive charge desorption plate (Thermo Fisher Scientific). Sections were stored at −80°C before further analysis. They were desiccated at −20°C for 1 hour and then at room temperature for 2 hours before mass spectrometry imaging (MSI) analysis. Meanwhile, an adjacent slice was left for H&E staining.

The analysis was performed as previously reported (18). In brief, this experiment was carried out with an ambient air flow–assisted desorption electrospray ionization-MSI platform (Beijing Victor Technology Co., LTD) in tandem with a Q-Orbitrap mass spectrometer (Q Exactive, Thermo Fisher Scientific). Here, the solvent formula was ACN/H_2O (8:2) at negative mode and ACN/H_2O (8:2, 0.1% formylic acid) at positive mode and the solvent flow rate was 5 μL/minute, the transporting gas flow rate was 45 L/minute, the spray voltage was set at 7 kV, and the distance between the sample surface and the sprayer was 3 mm as was the distance from the sprayer to the ion transporting tube. The MS resolution was set at 70,000, the mass range was 70 to 1,000 Da, the automated gain control target was 2×10^6, the maximum injection time was set to 200 ms, the S-lens voltage was 55 V, and the capillary temperature was 350°C. The MSI experiment was carried out with a constant rate of 0.2 mm/s continuously scanning the surface of the sample section in the x direction and a 100-μm vertical step in the y direction.

Spatial resolved transcriptomics and metabolomics analysis

Spatial transcriptomics analysis

Raw sequencing reads were analyzed and quality controlled by the spatial ranger pipeline provided by 10x Genomics. Preprocessing and quality control were performed according to the standard Scanpy pipeline (https://scanpy-tutorials.readthedocs.io/en/latest/spatial/basic-analysis.html). The spatial distribution of marker gene expression or signature activity was visualized using the scanpy.pl.spatial() function.

For public spatial transcriptomics data, we analyzed the CosMx dataset of non–small cell lung cancer (NSCLC) from (19) and the Visium HD dataset of colorectal cancer from 10x Genomics (https://www.10xgenomics.com/products/visium-hd-spatial-gene-expression/dataset-human-crc). We visualized the normalized counts of macrophage markers (*CD68* and *CD14*), angiogenic markers (*VEGFA* and *SLC2A1*), and MHC-II markers (*CD74* and *CIITA*) in the field of view 16 of sample lung 5-2 (replicate 2 of lung 5) and in the whole slide of sample P2 colorectal cancer using the function squidpy.pl.spatial_scatter().

Spatial metabolomics analysis

The collected .raw files were converted into .imzML format using imzMLConverter (RRID: SCR_021642) and then imported into MSiReader (an open-source interface to view and analyze high resolving power MS imaging files on the Matlab platform; ref. 20) for ion image reconstructions after background subtraction using the Cardinal (RRID: SCR_013422) software package. All MS images were normalized using total ion count normalization in each pixel (21). Region-specific MS profiles were precisely extracted by matching high–spatial resolution H&E images.

Point-to-point matching of paired spatial transcriptomics and spatial metabolomics

The method involves aligning images containing spatial transcriptomics information (e.g., H&E-stained images) with spatial

metabolomics images of adjacent serial sections to obtain spatial coordinate information of specific marker points. It then converts the spatial information from both datasets into a unified spatial coordinate system, calculates the final scaling factor and rotation angle, and uses these parameters to transform the spatial coordinates of the metabolomics data to match those of the transcriptomics data. Finally, it fits the spatial metabolomics data and associates them with the corresponding spots in the spatial transcriptomics data, summing the underlying pixel data to obtain the spatial metabolomics data corresponding to each spot in the spatial transcriptomics data. The aligned spatial metabolomics data were then imported into an AnnData object for integrated analysis with the corresponding spatial transcriptomics data using Scanpy (RRID: SCR_018139) and Squidpy (RRID: SCR_026157). Preprocessing and quality control of aligned spatial metabolomics data were performed according to the standard spatial metabolomics analysis pipeline MALDIpy (https://github.com/TheHumphreysLab/MALDIpy). The spatial distribution of metabolites was visualized using the scanpy.pl.spatial() function.

Integrative analysis of spatial multiomics

1) Modality integration:

To integrate information from spatial transcriptomics and spatial metabolomics within a unified spatial coordinate system, we employed MultiVI (22), a deep generative model for integrated analysis of multimodal data. Spatial multiomics data from two slides were merged into a single anndata object, with each spot containing gene and metabolite count information. Spots were categorized into three types: (i) those with paired transcriptomics and metabolomics data, (ii) those with transcriptomics data only, and (iii) those with metabolomics data only. The integration was performed using "modality" as the batch key and "sample" as the categorical covariate key, with the model parameter "n_latent" set to 30. The standard MultiVI tutorial (https://docs.scvi-tools.org/en/stable/tutorials/notebooks/multimodal/MultiVI_tutorial.html) was followed to train the model, resulting in joint embeddings for each spot in the multiomics latent space.

2) Multi-slide integrative spatial clustering:

To identify consistent spatial niches defined by multiomics features across two slides, we performed cross-slide clustering using CellCharter (23) v0.2.0. Based on the spatial network computed by the squidpy.gr.spatial_neighbors() function, we utilized the joint embeddings learned by MultiVI and performed neighborhood aggregation using cellcharter.gr.aggregate_neighbors(). This process involved concatenating the features of each spot with the features aggregated from neighboring spots across increasing layers. Following the standard procedure outlined in the CellCharter tutorial (https://cellcharter.readthedocs.io/en/latest/notebooks/codex_mouse_spleen.html), the optimal number of clusters was determined automatically. Subsequently, the scanpy.tl.rank_genes_groups() function was applied to identify feature genes for each spatial cluster, thereby defining the spatial niches. Differential metabolite abundance was analyzed using a custom Python script. Metabolite abundance in each cluster was compared with all other spots. LFC was calculated by taking the $\log_2$ of the ratio of mean abundance in the cluster to the mean abundance in the rest. *P* values were determined using the Wilcoxon rank-sum test and adjusted for FDR using the Benjamini–Hochberg method.

3) Macrophage abundance estimation:

To reliably estimate the spatial abundance of macrophages, the tool Cell2location (RRID: SCR_024859) v0.1.3 was employed to evaluate macrophage abundance in each spot on the two slides separately. The immune cell scRNA-seq reference data from the Cell2location tutorial was used as our reference, and the analysis was performed following the pipeline (https://cell2location.readthedocs.io/en/latest/notebooks/cell2location_tutorial.html). The specific parameters were set as follows: cell_count_cutoff = 5, "cell_percentage_cutoff2 = 0.03, nonz_mean_cutoff = 1.12, N_cells_per_location = 5, and detection_alpha = 200. The macrophage abundance was calculated by summing the abundances of "Macrophages_M1", "Macrophages_M2", and "Monocytes" in each spot. Spots with macrophage abundance greater than 0.1 were identified as "TAM spots".

4) Spatial cross-correlation analysis:

In aligned spatial multiomics, gene expression, metabolite abundance, and signature level can be mapped to the same spatial coordinate system, allowing for spatial correlation analysis between these variables. The binary adjacency weight matrix (W) was generated using Delaunay triangulation based on spatial connectivity, in which weights for spatially adjacent spots were set to 1 and non-neighbors to 0. Spatial cross-correlation was calculated using a custom Python script adapted from the "spatialCrossCor" and "spatialCrossCorTest" functions in the MERINGUE package v1.0 (24). The spatial cross-correlation index was defined according to the formula provided in the original article (24):

$$SCI = \frac{N}{2\sum_i^N \sum_j^N W_{ij}} \frac{\sum_i^N \sum_j^N W_{ij}\left(x_i - \bar{x}\right)\left(y_i - \bar{y}\right)}{\sqrt{\sum_i^N \left(x_i - \bar{x}\right)^2}\sqrt{\sum_i^N \left(y_i - \bar{y}\right)^2}}$$

in which N is the total number of spots, x represents the magnitude of a variable in a given spot i, and y represents the magnitude of another variable in a given spot j. When x in spot i is positively correlated with y in spot j's spatially adjacent neighbors, the spatial cross-correlation index for this pair of variables will be positive, and *vice versa*.

Cluster co-occurrence analysis

Cluster co-occurrence ratio was calculated using the function squidpy.gr.co_occurrence(). This ratio provides a score representing the co-occurrence of clusters of interest and is computed across increasing radii within the tissue area. It is defined as:

$$\frac{p(\exp \mid cluster)}{p(\exp)}$$

in which *cluster* is the annotation of interest used to condition the co-occurrence of all clusters, the $p(\exp \mid cluster)$ represents the probability of a specific cluster (exp) given the presence of the cluster of interest (*cluster*), and $p(\exp)$ denotes the overall probability of the specific cluster occurring across the entire sample.

Correlation analysis of macrophages' functional programs with effector signature in CD8$^+$ T cells

For correlation analysis between ISG, MHC-II, angiogenic, and lipid-associated program signatures in macrophages and effector T-cell

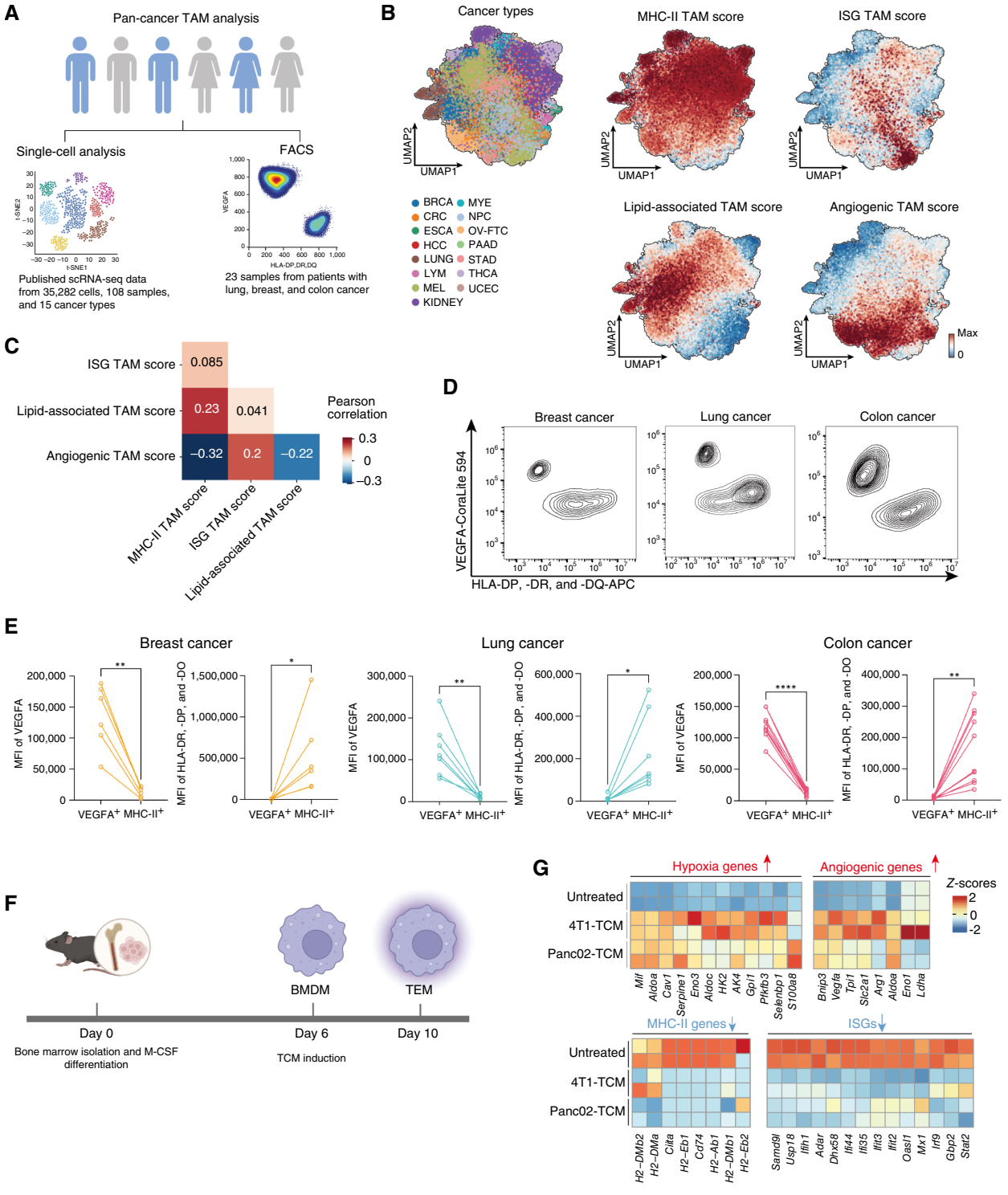

Figure 1.

Tumor-derived factors produce mutually exclusive phenotypes that represent TAMs in human cancers. **A,** Workflow of pan-cancer TAM analysis. **B,** Uniform Manifold Approximation and Projection (UMAP) of TAMs from 15 cancers, colored by signature scores (genes listed in Supplementary Table S1). **C,** Pairwise Pearson correlations among indicated signatures in (**B**) are displayed under FDR < 1×10^{-10}. **D** and **E,** FACS representative plots (**D**) and quantitative analysis (**E**) of VEGFA and MHC-II expression in TAMs from fresh tumors. **F,** Workflow for TEM generation. **G,** Heatmap of hypoxia, angiogenesis, MHC-II, and interferon genes in control and TEMs. *P* value was determined by a paired *t* test ($n = 6$–10 for each cancer type). *, $P < 0.05$; **, $P < 0.01$; (*Continued on the following page.*)

signature (*IFNG*, *GZMA*, *GZMB*, *PRF1*, and *TBX21*) in $CD8^+$ T cells, we analyzed scRNA-seq datasets spanning three cancer types: NSCLC (EMTAB6149, GSE117570, GSE127465, GSE131907, GSE139555, GSE143423, GSE150660, and GSE153935), head and neck squamous cell carcinoma (GSE139324), and non–Hodgkin lymphoma (GSE128531 and GSE147944; see Supplementary Table S7). Following preprocessing, quality control, dimension reduction, and cell type annotation of the datasets, we computed the arithmetic average of signatures in corresponding cell types at the patient sample level. Subsequently, linear regression was applied to these averages/percentages.

Experimental details related to *Adar* myeloid KO mice

Adoptive transfer of *Adar* myeloid KO HSCs (LSL-Cas9;Lyz2-Cre)

HSCs isolated from LSL-Cas9; Lyz2-Cre mice were transduced either with sgRNAs against either *Adar* or control (listed in Supplementary Table S2). These HSCs were then expanded and transferred into lethally irradiated $CD45.1^+$ recipient mice (n = 5–6). *Adar* myeloid KO (mKO; sg*Adar*-1) and control (sgNC) mice were subcutaneously injected with indicated tumor cells after 6 weeks of adoptive transfer of HSCs. The detailed procedures of viral infection and expansion of HSCs were described in the previous section "*In vivo* CROP-seq experiments".

Measurement of tumor growth curve

1×10^6 LLC and 1.5×10^6 B16F10 tumor cells were implanted subcutaneously into the flank of mice, respectively. The length (L) and width (W) of the tumors were measured starting at day 7 and every 3 days thereafter, and tumor volumes were calculated with formula $(L \times W^2)/2$. For anti–PD-1 treatment, mice bearing tumors were intraperitoneally injected either with 200 μg rat IgG (Bio X Cell, cat. #BE0094, RRID: AB_1107795) or 200 μg of anti–PD-1 antibodies (Bio X Cell, cat. #BE0273, RRID: AB_2687796) on days 4, 7, and 10 for B16F10.

Single-cell RNA processing and analysis

Quality control, dimension reduction, and clustering for scRNA-seq data followed the same strategy as detailed in the forementioned section "Single cell clustering and visualization".

CellPhone DB analysis

The cell–cell interaction analysis was performed by CellPhone DB (RRID: SCR_017054) v3.1.0 based on established receptor–ligand interactions between two cell types/subtypes. To calculate the null distribution of average ligand–receptor expression levels of the interacting clusters, cluster labels of all cells were randomly permuted for 1,000 times. Individual ligand or receptor expression was thresholded with a cutoff value based on the average log gene expression distribution for all genes across all the cell types. The significant cell–cell interactions were defined as P value < 0.05 and average log expression > 0.1.

Tumor-infiltrating lymphocyte analysis

Tumor tissues were processed into single cells as described in the previous section "Flow cytometric analysis of human TAMs". Cells were first stained with the Zombie-NIR Fixable Viability Kit (BioLegend, cat. #423106) in PBS and then stained with anti–mouse CD16/32 (BioLegend, cat. #101320, RRID: AB_1574975) to block the IgG Fc receptor. The cells were stained with surface markers, fixed, and permeabilized for intracellular staining.

The following antibodies were used: anti–mouse CD45 (BioLegend, cat. #103133, RRID: AB_10899570), anti–mouse CD45.2 (BioLegend, cat. #109813, RRID: AB_389210), anti–mouse CD3 (BioLegend, cat. #100204, RRID: AB_312661), anti–mouse CD8a (BioLegend, cat. #100708, RRID: AB_312747), anti–human/mouse CD11b (BioLegend, cat. #101205, RRID: AB_312788), anti–mouse Ly-6G/Ly-6C (Gr-1; BioLegend, cat. #108438, RRID: AB_2562215), anti–mouse LAG-3 (BioLegend, cat. #125210, RRID: AB_10639727), anti–mouse PD-1 (BioLegend, cat. #135216, RRID: AB_10689635), anti–granzyme B (BioLegend, cat. #372214, RRID: AB_2728381), anti–mouse arginase 1 (Thermo Fisher Scientific, cat. #17-3697-82, RRID: AB_2734835), anti–mouse I-A/I-E (BioLegend, cat. #107629, RRID: AB_2290801), anti–mouse CD64 (BioLegend, cat. #139314, RRID: AB_2563904), and anti–mouse CD40 (BioLegend, cat. #124609, RRID: AB_1134084). Beckman CytoFLEX S was used for data collection and FlowJo (RRID: SCR_008520) was used for data analysis.

Statistical analysis

Statistical analyses were carried out using GraphPad Prism 9 software (RRID: SCR_002798). We employed paired/unpaired Student t test, one-way ANOVA, or two-way ANOVA tests as indicated (ns, not significant; *, $P < 0.05$; **, $P < 0.01$; ***, $P < 0.001$; ****, $P < 0.0001$). For power analysis, the group sizes for *in vivo* experiments were empirically determined based on our previous experience with the corresponding tumor models. Likewise, group sizes for *in vitro* experiments were selected based on our prior understanding of the variability in the experiments.

Results

Tumor-derived factors produce mutually exclusive phenotypes that are highly conserved in human TAMs

To investigate the polarization mechanisms of TAMs, we analyzed scRNA-seq data from 108 samples across 15 cancer types and identified mutually exclusive gene programs: MHC-II/lipid metabolism and angiogenic signatures (**Fig. 1A–C**; Supplementary Fig. S1A). Next, flow cytometric validation in 23 patient-derived breast, colon, and lung cancer samples confirmed that VEGFA (angiogenic) and MHC-II were mutually exclusive in TAMs (**Fig. 1D** and **E**; Supplementary Fig. S1B and S1C). We assessed whether our findings aligned with known TAM subsets by analyzing angiogenic and MHC-II signatures in scRNA-seq data from human colorectal liver metastases (25). The heatmap revealed distinct distribution patterns between these two signatures across TAM subsets, supporting their mutual exclusivity (Supplementary Fig. S2A and S2B). Clinical correlation analysis using TCGA data showed that MHC-II programs were associated with better survival, whereas angiogenic programs showed the opposite effect (Supplementary Fig. S3). Together, our analysis suggests that the mutually exclusive nature of angiogenic and MHC-II programs is a widely conserved feature in TAMs.

(*Continued.*) ****, $P < 0.0001$. BRCA, breast cancer; CRC, colorectal cancer; ESCA, esophageal carcinoma; HCC, hepatocellular carcinoma; KIDNEY, kidney cancer; LUNG, lung cancer; LYM, lymphoma; Max, maximum; MEL, Melanoma; MFI, mean fluorescence intensity; MYE, myeloma; NPC, nasopharyngeal cancer; OV-FTC, ovarian or fallopian tube carcinoma; PAAD, pancreatic adenocarcinoma; STAD, stomach cancer; THCA, thyroid carcinoma; t-SNE, t-distributed stochastic neighbor embedding; UCEC, uterine corpus endometrial carcinoma. [**A** and **F,** Created in BioRender. Pan, D. (2025) https://BioRender.com/cby59e8]

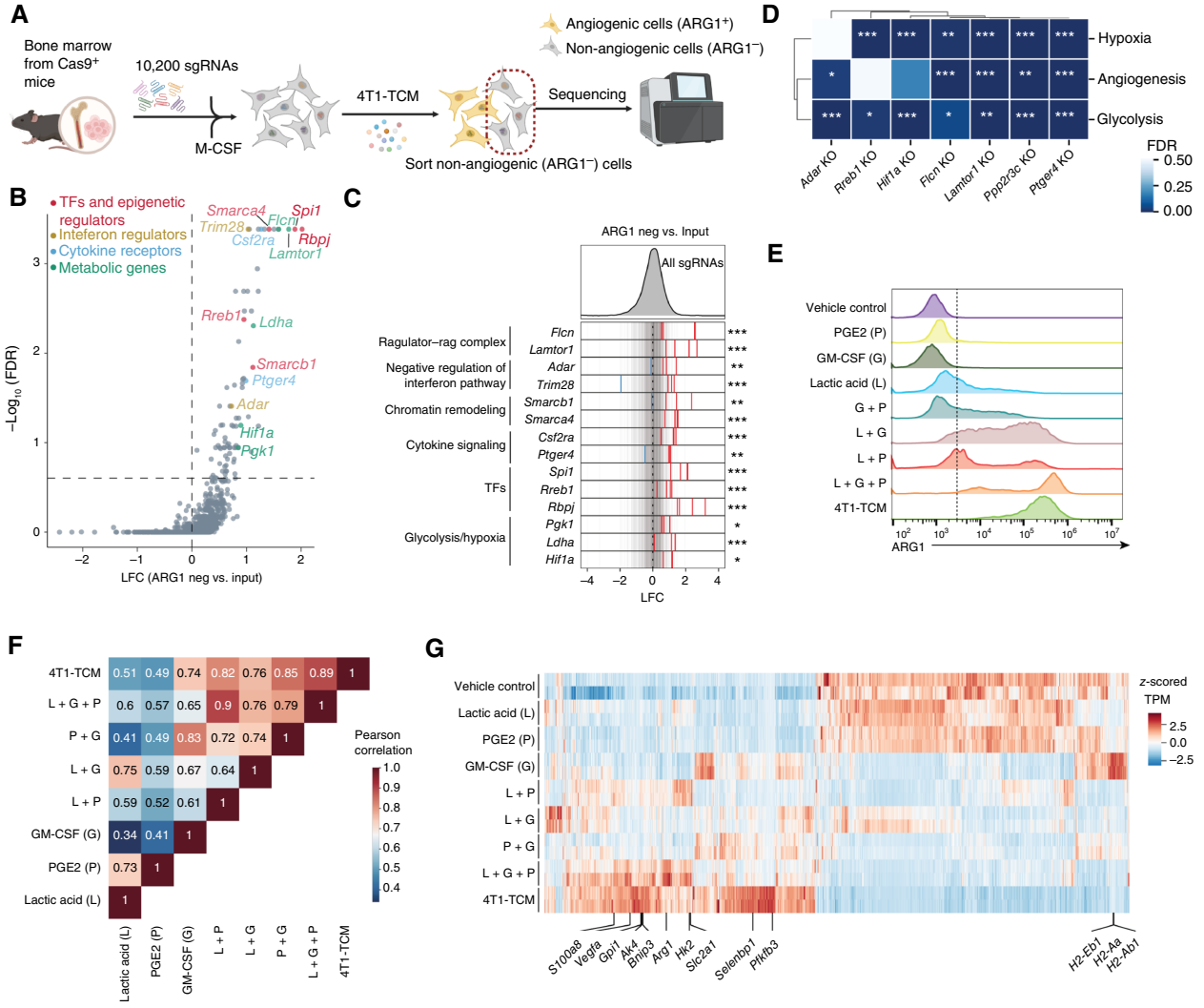

Figure 2.

Identification of tumor-derived factors essential for the generation of an angiogenic phenotype in macrophages. **A,** Workflow of CRISPR screening in 4T1-TCM–educated TEMs. **B** and **C,** LFC of top hits enriched in ARG1^{-} TEMs (**B**) and sgRNA distribution (red/blue: enriched/depleted targets; gray: controls) of CRISPR screen results. *, FDR ≤ 0.25; **, FDR ≤ 0.05; ***, FDR ≤ 0.01. **D,** Heatmap showing hypoxia/angiogenesis/glycolysis signatures in KO TEMs analyzed by top 200 downregulated genes. *, FDR < 0.05; **, FDR < 0.01; ***, FDR < 0.001. **E,** FACS quantification of ARG1 in macrophages treated with 25 mmol/L lactate, 100 nmol/L PGE2, or 2 ng/mL GM-CSF individually or in combinations. One of three independent experiments is shown. **F,** Pearson correlations (FDR < 0.05) between 4T1-TCM and LGP factor–treated BMDMs (G: GM-CSF; L: lactate; and P: PGE2). **G,** Expression levels (*z*-scores) of DEGs in 4T1-induced TEMs compared with control BMDMs (FDR < 0.05 and LFC > 1) under indicated conditions. Genes related to angiogenesis and MHC-II are highlighted. [**A**, Created in BioRender. Pan, D. (2025) https://BioRender.com/yb4u3jz]

To test whether tumor-derived factors induce TAM-like polarization, we generated TEMs by culturing BMDMs with conditioned media from 4T1 and Panc02 cancer lines (**Fig. 1F**). Bulk RNA-seq of these TEMs revealed significant upregulation of genes associated with hypoxia and angiogenesis (e.g., *Vegfa*, *Slc2a1*, and *Arg1*) in TEMs (**Figs. 1G**; Supplementary Fig. S4A). Conversely, genes involved in MHC-II (e.g., *H2-Aa*, *Cd74*, and *Ciita*) and interferon responses (e.g., *Isg15* and *Irf7*) were substantially downregulated, mimicking the mutually exclusive phenotypes observed in human TAMs (**Fig. 1G**; Supplementary Fig. S4A). Further analysis showed that TEMs derived from different tumor types consistently exhibited high expression of arginase 1 (ARG1), a key marker of angiogenic TAMs in murine models (Supplementary Fig. S4B). Functionally, these angiogenic TEMs demonstrated strong immunosuppressive properties, as their presence substantially inhibited proliferation of CD8^{+} T cells *ex vivo* (Supplementary Fig. S4C). Collectively, these data suggest that tumor-derived factors enhance the angiogenic program while concurrently inhibiting the interferon and MHC-II programs, reflecting the mutually exclusive functional phenotypes observed in human TAMs.

Identification of tumor-derived factors that are essential for generating the angiogenic phenotype in macrophages

To identify key regulators of tumor-induced TEM polarization into an angiogenic phenotype, we performed a large-scale *ex vivo* CRISPR screen. Bone marrow cells from Cas9 mice were infected

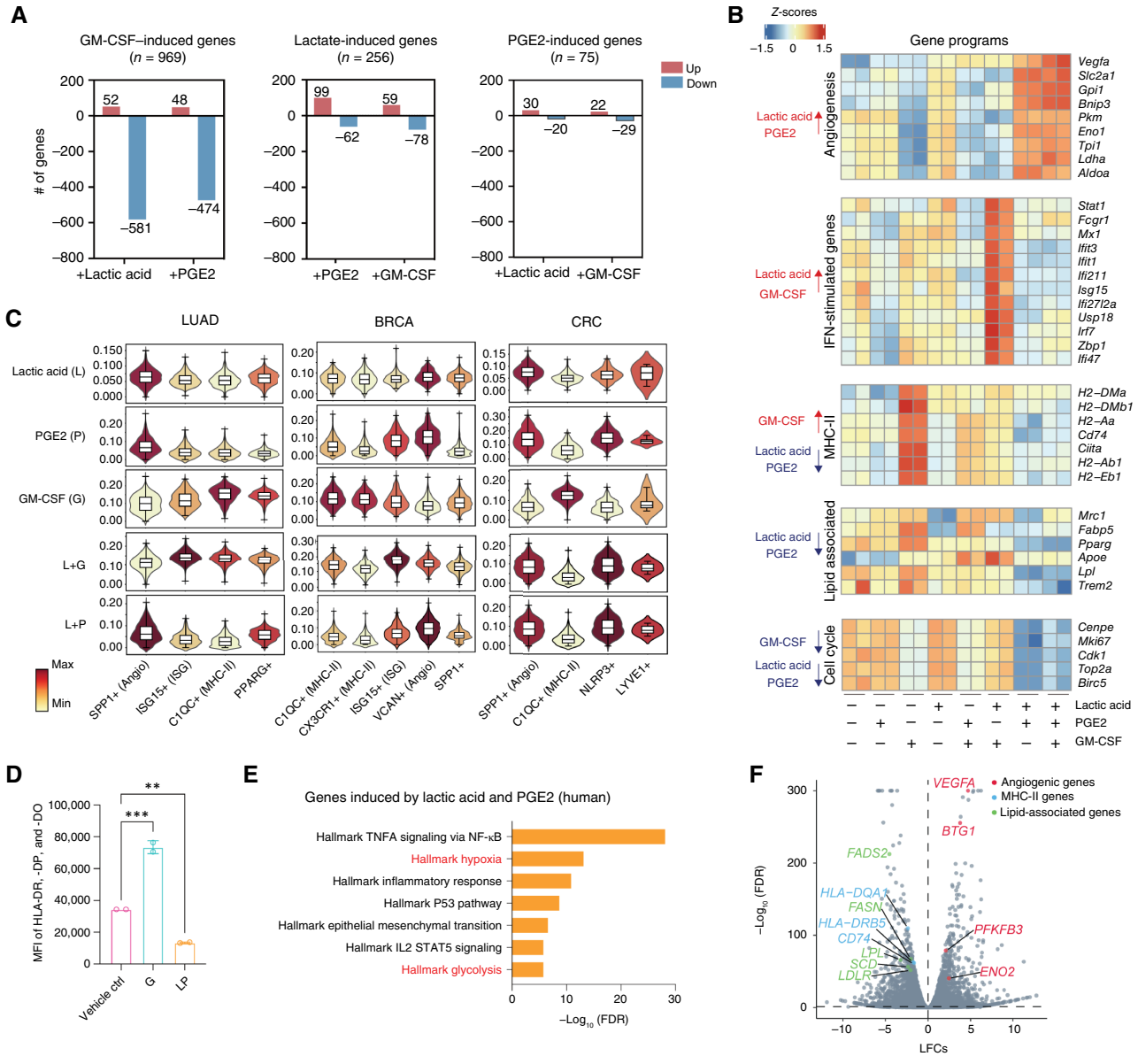

Figure 3.

Cooperative and antagonistic interactions among lactic acid, PGE2, and GM-CSF shape distinct gene programs in macrophages. **A,** RNA-seq analysis revealed cooperative and antagonistic gene regulation in BMDMs. GM-CSF (G)–induced genes ($n = 969$) were further upregulated by lactic acid (L; +52 genes) or PGE2 (P; +48) but downregulated (L: −581; P: −474). Similar analyses for L- and P-induced genes are shown in the middle and on the right. (Threshold: LFC > 1 and FDR < 0.05 vs. untreated). **B,** Expression levels of genes associated with specified functional programs in BMDMs following treatment with indicated combinations of GM-CSF, PGE2, and lactic acid. **C,** The expression levels of gene signatures induced by indicated conditions in BMDMs were plotted for each TAM subset from pan-cancer scRNA-seq analysis. Signature genes are defined as the top 50 significantly induced genes (ranked by LFC) by GM-CSF (G), lactic acid (L), PGE2 (P), and LP and LG in BMDMs (Supplementary Table S3). **D,** FACS quantification of HLA-DR/-DP/-DQ in human M-CSF–primed macrophages treated with G or LP. Data are represented as means ± SD. One of two representative experiments is shown. ($n = 2$ for each group). **E** and **F**, GSEA analysis (**E**) and volcano plot (**F**) showing induced and suppressed genes of human primary macrophages by LP. Related pathways were highlighted. *P* values determined by one-way ANOVA. **, $P < 0.01$; ***, $P < 0.001$. MFI, mean fluorescence intensity.

with an sgRNA library targeting 2,425 highly expressed genes in macrophages (Supplementary Table S8), and the cells were then further differentiated into TEMs using 4T1 TCM (**Fig. 2A**). Given that ARG1 is significantly upregulated in TEMs and is a recognized marker for the angiogenic phenotype in murine macrophages (Supplementary Fig. S4B; refs. 26, 27), we FACS sorted the ARG1-negative population, which represents cells with impaired polarization into the angiogenic state (Supplementary Fig. S5A). The screen revealed enriched regulators, including transcription factors (TF; *Spi1*, *Rreb1*, and *Rbpj*), hypoxia components (*Hif1a*), metabolic sensors (*Lamtor1* and *Flcn*), chromatin remodelers (SWI/SNF complex), and immune modulators (*Adar*, *Trim28*, *Ptger4*, and

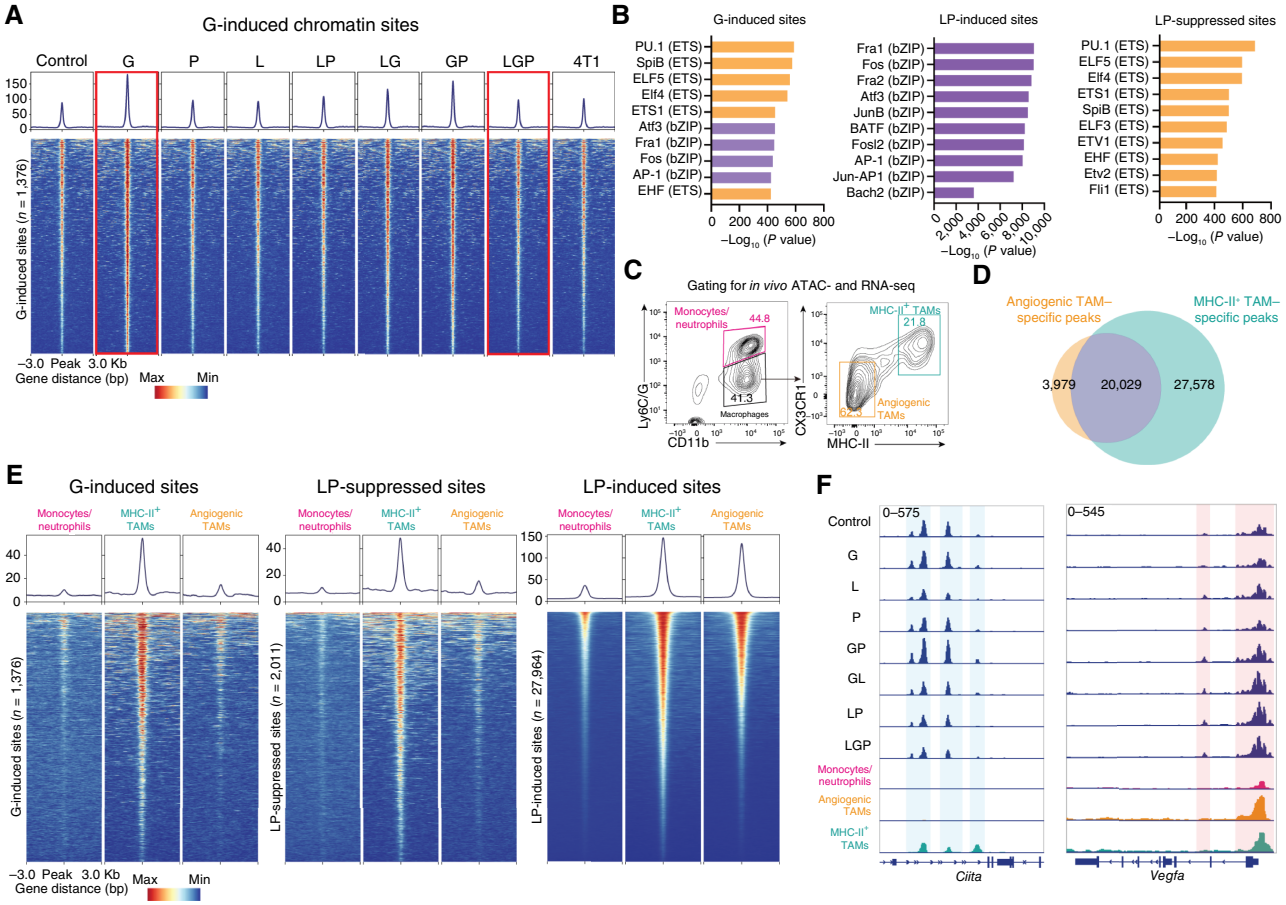

Figure 4.

LGP factors regulate specific subsets of chromatin sites that are related to MHC-II$^+$ and angiogenic TAMs *in vivo*. **A,** ATAC-seq heatmap of GM-CSF–induced chromatin sites ($n = 1{,}376$) in BMDMs treated with LGP alone or combinations (red boxes: LGP vs. G). **B,** HOMER motif analysis of top enriched TF binding sites in G-induced (left), LP-induced (middle), and LP-suppressed (right) regions. **C,** Gating strategy for sorting monocytes/neutrophils, angiogenic, and MHC-II$^+$ TAMs from 4T1 tumors (day 18–21after tumor inoculation) for multiomics. **D,** Venn diagram illustrating chromatin-accessible sites gained from angiogenic and MHC-II TAMs *in vivo*. **E,** Heatmap comparing *in vitro*–identified regulatory sites (G-induced and LP-modulated) with *in vivo* TAM epigenomes. **F,** Integrative Genomics Viewer tracks showing *Ciita* (MHC-II) and *Vegfa* (angiogenic) locus accessibility *in vitro* under indicated conditions and in 4T1 TAMs.

Csf2ra), demonstrating multilevel control of macrophage polarization by tumor-derived factors (**Fig. 2B** and **C**; Supplementary Table S9). This suggests that the polarization of macrophages by tumor cells is regulated at multiple levels.

To validate the screening results, we individually knocked out selected targets in TEMs and confirmed consistent downregulation of ARG1 (Supplementary Fig. S5B and S5C), demonstrating high reproducibility of our screen results. Bulk RNA-seq of these KO TEMs revealed reduced expression of angiogenesis-, glycolysis-, and hypoxia-related genes, indicating impaired angiogenic programs in these KO cells (**Fig. 2D**).

Lactic acid, PGE2, and GM-CSF are key mediators in the tumor-driven polarization of macrophages

To elucidate which tumor-derived factors drive the polarization of TEMs, we focused on receptors highlighted by our screen, particularly *Ptger4* (coding for the PGE2 receptor) and *Csf2ra* (for the GM-CSF receptor). To test whether tumor-derived PGE2 and GM-CSF drive this process, we generated *Cox2*-KO (PGE2-deficient) and *Csf2*-KO (GM-CSF–deficient) 4T1 cells (Supplementary Fig. S6A). As expected, conditioned media from these KO cells failed to induce ARG1 expression in TEMs, demonstrating that tumor-secreted PGE2 and GM-CSF are essential for establishing the angiogenic TEM phenotype (Supplementary Fig. S6B).

We then exposed BMDMs to recombinant GM-CSF and PGE2, both separately and in combination. ARG1 expression remained low under all these conditions, indicating that although PGE2 and GM-CSF are necessary, they are not sufficient on their own to induce ARG1 expression (**Figs. 2E**; Supplementary Fig. S6C). Previous studies have highlighted the crucial role of tumor-released lactic acid in inducing *Arg1* expression, primarily through activation of *Hif1a* (28), which was also identified as a major hit in our screen (Supplementary Fig. S5B and S5C). Therefore, we hypothesized that lactic acid might also be involved in polarization of TEMs. Remarkably, when BMDMs were co-treated with the combination of

lactic acid, GM-CSF, and PGE2, but not with any two factors alone, ARG1 expression reached levels comparable with those in TEMs induced by 4T1 cell–derived conditioned media, suggesting that all three factors together are required for effective polarization of macrophages by tumor cells (**Fig. 2E**; Supplementary Fig. S6C). RNA-seq further confirmed that co-treatment of three factors best mimicked the transcriptional profile of tumor-educated TEMs (**Fig. 2F** and **G**; Supplementary Fig. S6D), establishing lactic acid (L), GM-CSF (G), and PGE2 (P) as necessary and sufficient for angiogenic polarization., collectively referred to as LGP factors.

Cooperative and antagonistic interactions among lactic acid, PGE2, and GM-CSF shape distinct gene programs in TAMs

To better understand how LGP factors—lactic acid, GM-CSF, and PGE2—interact to shape the polarization of TEMs, we analyzed

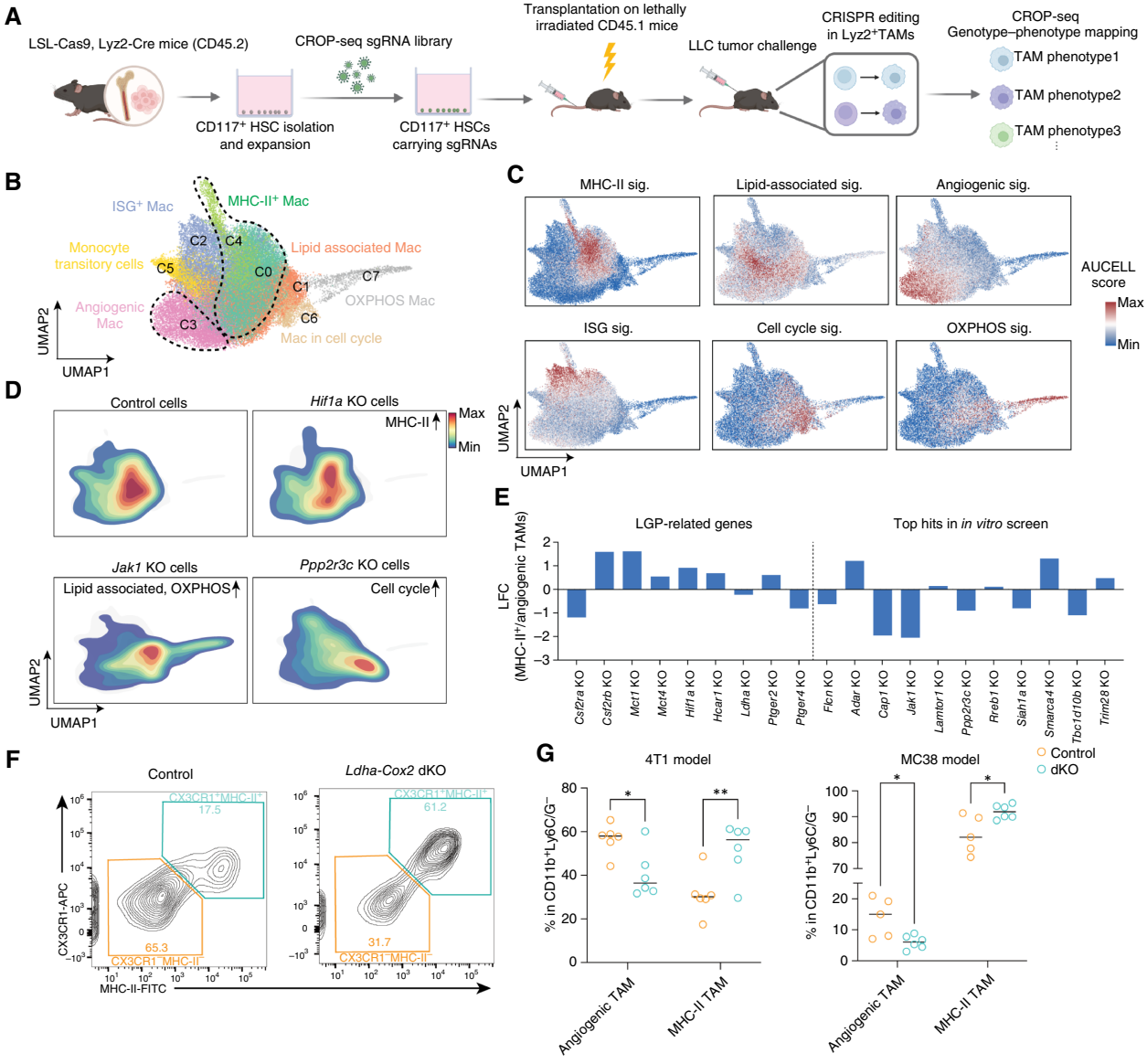

Figure 5.

LGP factors instruct the formation of mutually exclusive phenotype of TAMs in mouse models. **A,** Workflow of *in vivo* CROP-seq in TAMs. **B,** Uniform Manifold Approximation and Projection (UMAP) plot summarizing all cell states assessed in TAMs in the CROP-seq experiment. Functional phenotypes are annotated based on gene expression. **C,** UMAP showing the distribution of indicated gene programs in TAMs in the CROP-seq experiment. Genes in each program are described in Supplementary Table S6. **D,** Spatial distribution of sgRNA-targeted TAMs in UMAP space, highlighting phenotype enrichment. **E,** LFC in MHC-II$^+$/angiogenic TAM ratio following gene knockouts compared with control. **F,** Representative FACS plot showing the percentage of angiogenic and MHC-II subsets in TAMs from control and *Ldha/Cox2* dKO 4T1 tumors. **G,** Frequency of angiogenic and MHC-II subsets in TAMs from control and *Ldha/Cox2* dKO 4T1 (left) or MC38 (right) tumors ($n = 6$ for each group). Bars represent median. One of two representative experiments is shown. *P* values determined by two-way ANOVA. *, $P < 0.05$; **, $P < 0.01$. Mac, macrophage; Max, maximum; Min, minimum; sig, signature. [**A**, Created in BioRender. Pan, D. (2025) https://BioRender.com/8mjns7t]

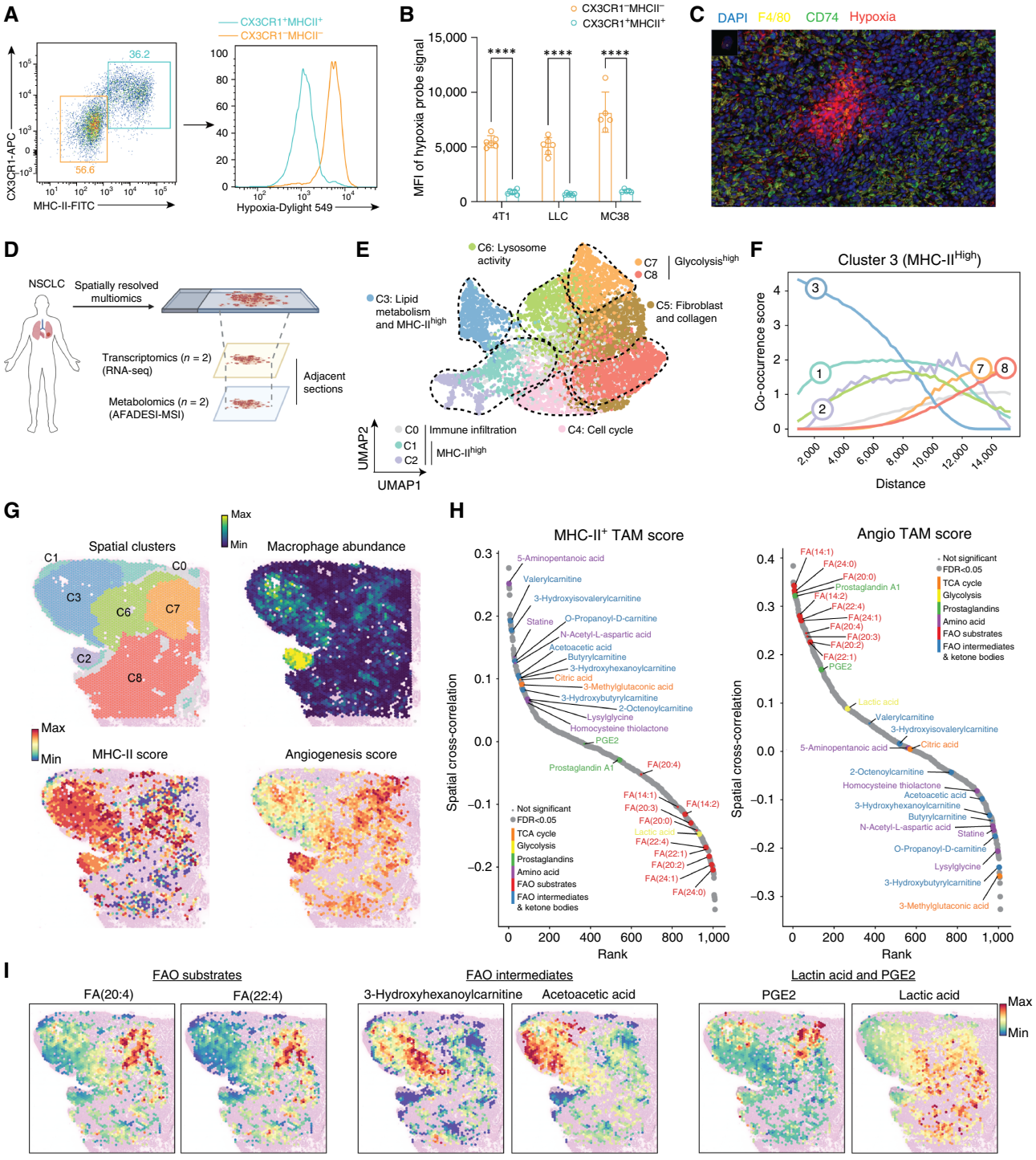

Figure 6.

Spatially resolved multiomics link TME metabolites to the niche-specific phenotype of TAMs in human cancer. **A,** Representative FACS analysis of hypoxia in CX3CR1^{+}MHCII^{+} and CX3CR1^{-}MHCII^{-} TAMs from 4T1 tumors. **B,** Bar plot showing the hypoxia level detected by intracellular staining of pimonidazole in CX3CR1^{-}MHCII^{-} and CX3CR1^{+}MHCII^{+} TAMs from 4T1, LLC, and MC38 tumors (n = 6 for each group). Data are represented as means ± SD. One of two representative experiments is shown. **C,** Multicolor immunofluorescence of angiogenic/MHC-II signatures in 4T1 tumors: hypoxia probe (red), CD74 (green), F4/80 (yellow), and DAPI (blue). **D,** Spatially resolved transcriptomics paired metabolomics workflow in human NSCLC samples. **E,** Uniform Manifold Approximation and Projection (UMAP) plot of spatially resolved multiomics spots integrated from two NSCLC samples. Color reflects different functional clusters of all Visium spots (see "Materials and Methods"). **F,** Co-occurrence score computed for all clusters in sample LUAD#1, conditioned on the presence of the cluster 3 (MHC-II^{high} niche). Numbers and colors refer to cluster identity. **G,** Spatial niches corresponding to the clusters shown in (**E**). (*Continued on the following page.*)

their potential interactions using RNA-seq data and observed both cooperative and antagonistic effects. For example, among GM-CSF–induced genes ($n = 969$), lactic acid and PGE2 downregulated the majority (581 and 474, respectively), including MHC-II–associated genes (e.g., *Cd74* and *Ciita*), whereas only a small fraction ($n = 52$ and 48, respectively) was further upregulated by these two factors, suggesting that lactic acid and PGE2 strongly antagonize GM-CSF (**Fig. 3A**; Supplementary Fig. S7A and S7B). In comparison, among the genes induced by lactic acid ($n = 256$), the combination of PGE2 and lactic acid further induced 99 genes, including angiogenesis-associated genes (e.g., *Arg1* and *Vegfa*), while repressing 62 others under the same conditions (**Fig. 3A**; Supplementary Fig. S7C), suggesting an overall cooperative effect between lactic acid and PGE2.

Strikingly, genes regulated by different combinations of these factors were enriched in distinct functional phenotypes commonly found in TAMs. For example, PGE2 and lactic acid cooperatively induced genes related to glycolysis and hypoxia pathways (e.g., *Arg1*, *Vegfa*, and *Slc2a1*; **Fig. 3B**; Supplementary Fig. S7D). Conversely, genes related to MHC-II (e.g., *Cd74* and *H2-Aa*), lipid metabolism (e.g., *Apoe* and *Trem2*), and cell cycle (e.g., *Mki67* and *Top2a*) were strongly repressed by the combination of lactic acid and PGE2 (**Fig. 3B**; Supplementary Fig. S7D and S7E). Of note, even though MHC-II closely associated lipid-associated program could also be suppressed by lactic acid and PGE2, its formation is independent with GM-CSF based on RNA-seq data (**Fig. 3B**). We observed that GM-CSF and lactic acid cooperatively induced many ISGs, such as *Ifi44*, *Ifi209*, and *Mx1* (**Fig. 3B**; Supplementary Fig. S7F). These findings highlight that the cooperative and antagonistic interactions among LGP factors could generate several major phenotypes associated with TAMs.

To determine the relevance of LGP-induced gene expression program in human context, we plotted the LGP factor–induced gene expression signatures (Supplementary Table S3) in human TAMs (7). Consistent with our *ex vivo* observations, MHC-II$^+$ TAMs exhibited high levels of GM-CSF signature genes and low levels of lactic acid and PGE2 (LP) signature genes, whereas angiogenic TAMs showed high levels of LP signature genes (**Fig. 3C**; Supplementary Fig. S7G). In contrast, ISG$^+$ TAMs displayed a mix of signatures from both GM-CSF and lactic acid/PGE2 (**Figs. 3C**; Supplementary Fig. S7G), suggesting that LGP factors generated gene expression signatures that are highly relevant in human TAMs.

Human macrophage validation further confirmed the conserved role of LGP factors in macrophage phenotype modulation. In donor-derived macrophages, GM-CSF upregulated MHC-II whereas LP suppressed it (**Fig. 3D**). Additionally, RNA-seq analysis revealed that the treatment of LP strongly induced the angiogenic gene expression program while suppressing MHC-II and lipid-associated genes (**Fig. 3E** and **F**), suggesting that LGP factors have conserved roles in regulating these pathways in human macrophages.

LGP factors regulate specific subsets of open chromatin sites in the angiogenic and MHC-II$^+$ TAMs, respectively

To better understand the complex interactions of LGP factors, we performed ATAC-seq on BMDMs treated with all combinations of LGP. Consistent with our RNA-seq findings, GM-CSF induced the accessibility of 1,376 chromatin sites, and the presence of LP (lactic acid and PGE2) significantly reduced the accessibility of these sites (**Fig. 4A**). Additionally, the combination of lactic acid and PGE2 suppressed 2,011 chromatin sites that were more accessible under GM-CSF treatment alone (Supplementary Fig. S8A), again highlighting an antagonistic relationship between GM-CSF and LP at the chromatin level. To explore the transcriptional activity regulated by these factors, we analyzed the enrichment of TF motifs across different LGP combinations. GM-CSF treatment–induced open chromatin sites associated with the bZIP (e.g., AP-1 and Fos) and ETS (e.g., PU.1 and ERG) TF families (**Fig. 4B**). Strikingly, LP treatment strongly suppressed chromatin sites associated with ETS family (**Fig. 4B**), suggesting that LP may selectively repress a subset of ETS-regulated genes that are activated by GM-CSF.

To assess the relevance of these LGP-regulated chromatin sites in TAMs *in vivo*, we performed ATAC-seq and RNA-seq on monocyte/neutrophil and TAM subsets sorted from the 4T1 tumor model (**Fig. 4C**). To sort live cells for this assay, we avoided using intracellular marker for cell staining. According to gene expression analysis in our in-house scRNA-seq data and previous literature (9), we chose CX3CR1 and MHC-II for TAM sorting, including MHC-II (CX3CR1$^+$MHC-II$^+$) and angiogenic TAMs (CX3CR1$^-$MHC-II$^-$; Supplementary Fig. S8B). Functional enrichment analysis of RNA-seq data confirmed that the sorted CX3CR1$^-$MHC-II$^-$ subsets were more angiogenic compared with MHC-II$^+$ TAMs (Supplementary Fig. S8C). Notably, a large number of chromatin sites ($n = 27{,}578$) were more accessible in MHC-II$^+$ TAMs compared with angiogenic TAMs, whereas only a limited set ($n = 3{,}979$) of chromatin sites showed greater accessibility in angiogenic TAMs (**Fig. 4D**). This suggests that MHC-II$^+$ TAMs are in a more "permissive" chromatin state, potentially making them more plastic in phenotypes.

We then examined the relevance of LGP-regulated chromatin sites in TAMs isolated from tumors in mouse models. Our analysis of TAMs revealed that GM-CSF–induced chromatin sites were more accessible in MHC-II$^+$ TAMs, whereas LP-suppressed sites were largely closed in angiogenic TAMs (**Fig. 4E**). In comparison, chromatin sites upregulated by LP were similarly accessible in both TAM subsets (**Fig. 4E**). Similar findings were observed in TAMs isolated from MC38 models (Supplementary Fig. S8D), suggesting that LP selectively suppresses a subset of chromatin sites in angiogenic TAMs, whereas GM-CSF enhances the accessibility of certain chromatin sites in MHC-II$^+$ TAMs, aligning with our *in vitro* observations.

Next, we analyzed the accessibility of specific genes related to functional phenotypes in TAMs and observed distinct accessibility patterns across different functional categories. For instance, genes linked to the MHC-II programs were highly accessible in MHC-II$^+$ TAMs, whereas these sites were completely closed in angiogenic TAMs (**Fig. 4F**; Supplementary Fig. S8E). Conversely, genes involved in hypoxia-related processes such as glycolysis and angiogenesis were equally accessible in both MHC-II$^+$ and angiogenic subsets (**Fig. 4F**; Supplementary Fig. S8E). Some ISGs, such as *Isg15*

(*Continued.*) Macrophage abundance estimated by cell2location. MHC-II and angiogenesis score distribution in TAM-enriched spots were shown. **H,** Rank plots display metabolite enrichment (angiogenic TAMs) and depletion (MHC-II TAMs), colored by type. Dots indicate significance (large: both samples; small: others). Spatial cross-correlation reflects mean values from two samples. **I,** Spatial distribution of representative metabolites in LUAD #1 sample. *P* value determined by two-way ANOVA. ***, $P < 0.001$. FAO, fatty acid oxixidation molecule; Max, maximum; MFI, mean fluorescence intensity; Min, minimum. [**D**, Created in BioRender. Pan, D. (2025) https://BioRender.com/8m1p2ip]

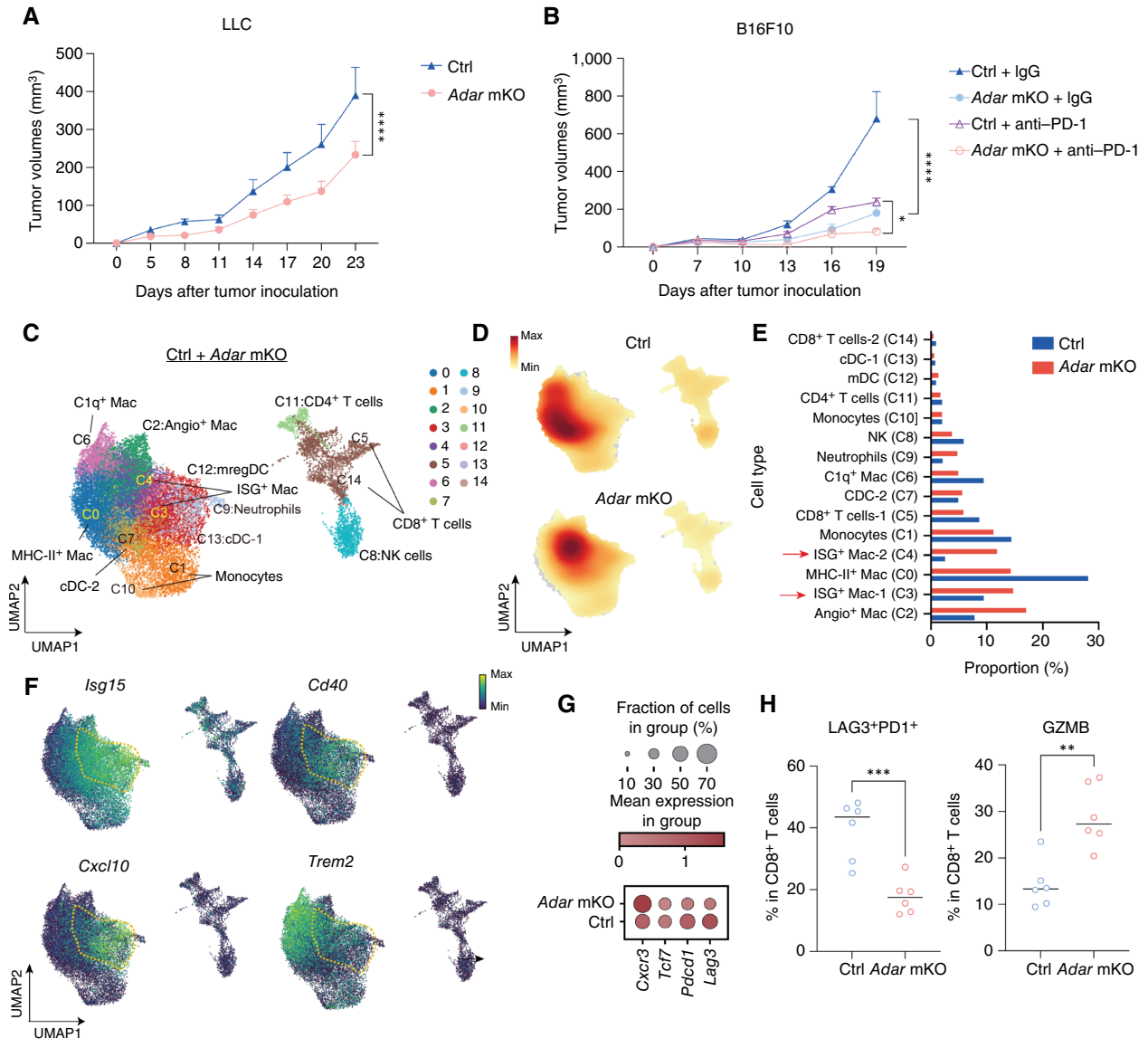

Figure 7.

Redirecting TAMs to ISG phenotype potentiates antitumor immunity. **A** and **B,** Control and *Adar* mKO mice were subcutaneously inoculated with 1×10^6 LLC cells (**A**) or 1.5×10^6 B16F10 cells (**B**), respectively ($n = 5$–6). **C,** Uniform Manifold Approximation and Projection (UMAP) plot displaying 15 subpopulations of tumor-infiltrating immune cells in control and *Adar* mKO mice based on scRNA-seq experiment. **D,** Density plot illustrating the distribution of immune cells isolated from control or *Adar* mKO mice based on scRNA-seq experiment. **E,** Horizontal bar plot depicting the fraction of tumor-infiltrating immune cell subpopulations ($CD45^+$) in control and *Adar* mKO mice, representing the differences in immune subpopulation proportions. **F,** Uniform Manifold Approximation and Projection plots showing the expression of indicated genes in the myeloid cluster based on scRNA-seq experiment. Yellow dashed lines indicate the region of ISG program in the Uniform Manifold Approximation and Projection. **G,** Dot plot of scRNA-seq depicting the mean expression levels of *Cxcr3*, *Tcf7*, *Pdcd1*, and *Lag3* in $CD8^+$ T cells between control and *Adar* mKO mice. **H,** Frequency of $LAG3^+PD1^+$ exhausted marker and GZMB effector marker in total $CD8^+$ T cells ($n = 6$ for each group). For panel (**A**) and (**B**), data are represented as means ± SEM. *P* value was determined by two-way ANOVA. One of two independent experiments is shown. For panel (**H**), bars represent median. *P* value was determined by an unpaired *t* test; one of two independent repeats is shown. *, $P < 0.05$; **, $P < 0.01$; ***, $P < 0.001$; ****, $P < 0.0001$. Ctrl, control; DC, dendritic cell; Mac, macrophage; Max, maximum; min, minimum.

and *Irf7*, showed similar accessibility in both subsets, suggesting that ISGs may be less suppressed in angiogenic TAMs (Supplementary Fig. S8E). Taken together, these distinct patterns of chromatin accessibility underscore the crucial role of LGP-regulated chromatin dynamics in shaping distinct phenotypes in TAMs *in vivo*.

LGP factors in the TME dictate the formation of specific TAM phenotypes in mouse models

To investigate LGP factors and other candidates in TAM regulation *in vivo*, we performed focused CRISPR screens using CROP-seq (29). Using the chimeric immune editing protocol (15,

16), we transplanted CRISPR-edited c-Kit$^+$ HSCs from LSL-Cas9; Lyz2-Cre mice into lethally irradiated mice (**Fig. 5A**; see "Materials and Methods" section). Upon LLC tumor challenge, most tumor-infiltrating immune cells were donor-derived (CD45.2$^+$), with no significant differences in immune cell composition between wild-type and chimeric mice (Supplementary Fig. S9A–S9C). To validate KO efficiency, we targeted SIRPα and observed about 78% reduction in TAMs from sg*Sirpa* chimeric mice versus controls (Supplementary Fig. S9D and S9E), confirming robust *in vivo* editing of our approach.

We designed two customized sgRNA libraries, including top hits identified from *in vitro* CRISPR screens and genes related to receptors of LGP factors (Supplementary Tables S4 and S5). After quality control, we retained a total of 47,856 cells from TAMs (CD11b$^+$ Ly6C/G$^-$ GFP$^+$) and identified eight distinct clusters using the *Leiden* algorithm (**Fig. 5B**; Supplementary Fig. S9F; ref. 30). This analysis confirmed major TAM signature gene expression programs, with angiogenic and MHC-II programs again exhibiting mutually exclusive distributions (**Fig. 5B** and **C**). Interestingly, targeting several top screening candidates led to dramatic alterations in TAM functional phenotypes. For example, knockout of *Hif1a*, a central regulator of hypoxia and angiogenic signaling, enriched MHC-II TAMs *in vivo* (**Fig. 5D**). Knockout of *Jak1* triggered an upregulation of genes associated with oxidative phosphorylation (**Fig. 5D**). Knockout of *Ppp2r3c*, a poorly characterized phosphatase in macrophages, significantly enhanced proliferating macrophages (**Fig. 5D**), suggesting its crucial role in controlling the cell cycle in TAMs.

With regard to LGP factor–related genes, knockout of *Csf2ra,* encoding the receptor for GM-CSF, decreased the MHC-II/angiogenic ratio as expected (**Fig. 5E**). *Csf2rb* KO did not recapitulate the phenotype of *Csf2ra*, possibly because of its role in other receptor heterodimers, such as IL3 and IL5 heterodimeric receptors (31). Conversely, knocking out genes encoding for LP receptors slightly increased the MHC-II/angiogenic ratio, consistent with their roles in regulating angiogenic programs *in vitro* (**Fig. 5E**). However, individual gene knockouts of these LP receptors only modestly affected the MHC-II/angiogenic ratio, likely because of the presence of multiple receptors for lactic acid (32) and PGE2 (33), and knocking out of any single receptor is insufficient to completely abolish their signal transductions.

To further explore whether tumor-derived LGP factors influence the polarization of MHC-II/angiogenic TAMs, we knocked out *Ldha* and *Cox2* (double KO, dKO), the key enzymes responsible for producing lactic acid and PGE2, respectively. We confirmed that the dKO cells produced substantially less amount of lactic acid and PGE2 (Supplementary Fig. S9G and S9H). Remarkably, in both the 4T1 and MC38 models, dKO tumors showed increased MHC-II$^+$ TAMs and decreased angiogenic (CX3CR1$^-$MHC-II$^-$) TAMs compared with controls (**Fig. 5F** and **G**; Supplementary Fig. S9I), demonstrating that tumor-intrinsic LP production critically dictates TAM subsets.

Niche-specific metabolic features correlate with spatially distinct TAM phenotypes in the TME

Given that the "LGP" factors are likely enriched in specific spatial regions within the TME, we hypothesized that distinct TAM phenotypes are determined by their spatial distribution. To this end, we used a hypoxia probe to label TAMs in hypoxic areas, in which lactic acid is highly abundant (34). Remarkably, in various tumor models (4T1, LLC, and MC38), only the angiogenic (CX3CR1$^-$MHC-II$^-$) TAMs, not the MHC-II$^+$ TAMs, stained positively with the hypoxia probe, indicating that angiogenic TAMs reside in hypoxic niches, whereas MHC-II$^+$ TAMs are found in normoxic areas (**Fig. 6A** and **B**; Supplementary Fig. S10A and S10B). Immunofluorescence confirmed this spatial segregation (**Fig. 6C**; Supplementary Fig. S10C and S10D), indicating that MHC-II$^+$ and angiogenic TAMs are not only mutually exclusive but also occupy distinct spatial niches.

To better understand the relationship between TME metabolites (e.g., lactic acid and PGE2) and macrophage phenotypes in human cancers, we conducted spatially resolved transcriptomics and metabolomics (ambient air flow–assisted desorption electrospray ionization-MSI) using tumors isolated from two patients with NSCLC (**Fig. 6D**). We first identified spatially distinct transcriptional and metabolic features within the TME by leveraging a spatial multiomics embedding learned through MultiVi (22) and employing CellCharter (**Fig. 6E**; ref. 23). We have identified cell neighborhoods characterized by high angiogenesis/glycolysis (clusters 7 and 8) and high MHC-II expression (Clusters 3; **Fig. 6E**; Supplementary Fig. S11A). Further analysis showed that the MHC-II–high neighborhood (cluster 3) had a lower co-occurrence score with glycolysis neighborhoods (clusters 7 and 8) at shorter distances, suggesting spatial exclusivity between MHC-II$^+$ and glycolysis niches (**Fig. 6F**). By analyzing publicly available spatial transcriptomic data from lung and colon cancer samples, we confirmed that angiogenic (*VEGFA* and *SLC2A1* high) and MHC-II (*CD74* and *CIITA* high) signatures are distributed in spatially distinct niches (Supplementary Fig. S11B and S11C), consistent with our dataset. Furthermore, by analyzing spatial spots with abundant macrophage signals (see "Materials and Methods"), we found that the spatial distribution of MHC-II and angiogenic expression signatures was mutually exclusive within these spots (**Fig. 6G**; Supplementary Fig. S11D–S11F), reinforcing that MHC-II$^+$ and angiogenic TAMs occupy distinct spatial niches.

We then examined the spatial co-localization of metabolic features and specific macrophage gene expression signatures. Notably, specific metabolic patterns were strongly correlated with TAM gene signatures. For example, MHC-II gene programs were associated with an enhanced fatty acid oxidation (FAO) signature, with an enrichment of FAO intermediates, including ketone bodies, acetoacetic acid, 3-hydroxyhexanoylcarnitine, and valerylcarnitine, whereas FAO substrates (e.g., fatty acids) were depleted in MHC-II^{high} neighborhoods (**Fig. 6H** and **I**). In contrast, angiogenic TAM niches exhibited low FAO activity, as indicated by fewer FAO intermediates and a higher amount of FAO substrates (**Fig. 6H** and **I**). Importantly, the angiogenic TAM niches also showed increased levels of glycolysis products like lactic acid and high concentrations of prostaglandins (PGA1 and PGE2; **Fig. 6H** and **I**). Taken together, these results reveal a spatial link between metabolites and TAM programs, supporting our finding that PGE2 and lactic acid promote angiogenesis and suppress MHC-II.

Rewiring TAMs to ISG phenotype potentiate antitumor immunity

Finally, we investigated which functional phenotype in macrophages is linked to better outcomes in antitumor immunity. Using scRNA-seq data from multiple cancer cohorts, we analyzed the correlation between each TAM signature and the effector signature (*GZMB*, *GZMA*, *PRF1*, *IFNG*, and *TBX21*) in CD8$^+$ T cells. Neither the angiogenic nor the MHC-II$^+$ phenotypes correlated with the effector CD8$^+$ T-cell signature. In contrast, the ISG signature in TAMs consistently exhibited a high correlation with the effector

signature in T cells across multiple cancer types (Supplementary Fig. S12). This suggests that the ISG program in macrophages is associated with a better functional state of T cells.

In light of this discovery, we found that knocking out *Adar*, an RNA-editing enzyme and a top hit from our *in vitro* screen, significantly enhanced the expression of ISGs in TEMs (Supplementary Fig. S13A and S13B). We then evaluated the function of *Adar*-deficient macrophages by coculturing them with splenocytes. *Adar* knockout in macrophages partially rescued the suppression of $CD8^+$ T-cell proliferation mediated by macrophages, confirming the functional role of *Adar* KO in macrophages *in vitro* (Supplementary Fig. S13C). To further assess the functional impacts of KO *Adar* in macrophages *in vivo*, we generated *Adar* mKO mice by reconstituting lethally irradiated mice with LSL-Cas9; Lyz2-Cre HSCs expressing sgRNA against *Adar* or a control sgRNA. In the LLC tumor model, *Adar* mKO mice exhibited significantly slower tumor growth compared with controls (**Fig. 7A**). Furthermore, *Adar* mKO also slowed tumor growth in the B16F10 model and enhanced the efficacy of anti–PD-1 treatment (**Fig. 7B**), suggesting that inactivation of *Adar* in $Lyz2^+$ myeloid cells substantially potentiate antitumor immunity.

To evaluate the impact of ISG^+ TAMs on antitumor immunity and the broader TME, we conducted scRNA-seq on total $CD45^+$ cells from LLC tumors in control and *Adar* mKO mice. This analysis identified 15 clusters, covering major myeloid and lymphoid subsets (**Fig. 7C**; Supplementary Fig. S13D). Notably, we observed significant myeloid lineage alterations within tumors isolated from *Adar* mKO mice, with a substantial enrichment of two ISG^+ TAM subsets (C3-4; **Fig. 7D** and **E**). We also found that *Adar* showed the highest expression level in ISG^+ TAMs among the myeloid compartment in control mice, further highlighting its critical regulatory role in ISG^+ TAMs (Supplementary Fig. S13E). Interestingly, angiogenic TAMs were more abundant in the TME of *Adar* mKO mice (**Fig. 7C**). This could be due to a closer relationship between ISG^+ and angiogenic TAMs, as suggested by trajectory analysis (Supplementary Fig. S13F).

In particular, ISG^+ TAMs exhibited elevated expression of T cell–recruiting chemokines (*Cxcl9* or *Cxcl10*), the costimulatory gene *Cd40*, and low expression of *Trem2* (**Fig. 7F**). Consistently, *CD40*, *CXCL10/11*, and *FCGR1A* are also highly expressed in ISG^+ TAMs as compared with other TAM subsets in human cancers (Supplementary Fig. S14A; refs. 7, 10). We performed FACS analysis of TAMs and confirmed that there was an enrichment of ISG^+ TAMs ($CD40^+$ $CD64^+$) in *Adar* mKO tumors (Supplementary Fig. S14B).

Given the high expression of immune-stimulatory molecules, we used CellPhone DB (35) to analyze myeloid–T-cell interactions and found enhanced CXCL10–CXCR3 and CD40–CD40L signaling in *Adar* mKO tumors, suggesting stronger immune stimulation (Supplementary Fig. S14C). Furthermore, scRNA-seq and flow cytometry revealed fewer exhausted ($LAG3^+$ $PD\text{-}1^+$) and more cytotoxic ($GZMB^+$) $CD8^+$ T cells in *Adar* mKO tumors compared with controls (**Fig. 7G** and **H**). These results indicate that *Adar* deletion reshapes TAMs into an ISG^+ state, boosting T cell–mediated antitumor immunity.

Discussion

TAMs exhibited diverse functional phenotypes, but the conserved mechanisms guiding these phenotypes remain elusive. Here, we identified two mutually exclusive programs in TAMs: the angiogenic program and the MHC-II^+ program, which are highly conserved across various murine and human cancers (7, 9). Although scRNA-seq studies describe these programs using different markers [e.g., $SPP1^+/C1Q^+$(7) vs. $PTGS2^+/C1Q^+$(9)] because of tumor heterogeneity, this mutual exclusivity unifies prior classifications and establishes a consistent framework for TAM research across cancers.

Due to technical limitations in large-scale CRISPR screens of TAMs, we used TEMs to reveal GM-CSF as a driver of MHC-II programs, whereas lactic acid and PGE2 induce angiogenic programs and suppress MHC-II, establishing their striking antagonism, with chromatin accessibility patterns mirroring this mutual exclusion. Notably, the MHC-II program consistently associates with lipid metabolism genes (7) and opposes the angiogenic program, supporting our LGP polarization model that explains conserved TAM phenotypic exclusion across cancers. Our LGP model also explains how local metabolic conditions dictate TAM localization and function. Spatial analysis of NSCLC revealed angiogenic TAMs clustered in lactic acid/PGE2-rich, hypoxic regions with high glycolysis, whereas MHC-II^+ TAMs occupied areas with active FAO. This demonstrates metabolic regulation of TAM polarization. Current spatial transcriptomics limitations prevented GM-CSF detection, necessitating higher-resolution techniques like MERFISH for future validation. Additionally, Cortese and colleagues (25) similarly identified spatially segregated TAM subsets in colorectal cancer, supporting our model.

Collectively, our study establishes a model in which tumor microenvironmental factors drive conserved TAM functional programs. The two major phenotypes—angiogenic and MHC-II TAMs—can be further divided into subtypes such as $FOLR2^+$ and $TREM2/CARM^+$ populations (36). Although lactic acid, PGE2, and GM-CSF form the core LGP regulatory axis, other cytokines (37), hypoxia (28), and metabolites (38) also contribute to the macrophage polarization process. For example, TNFα may fine-tune TAM phenotypes, as seen with $IL1\beta^+$ angiogenic TAMs in hypoxic niches (39). This framework provides a mechanistic understanding of TAM diversity and plasticity across tumors.

Our scRNA-seq analysis identified ISG^+ TAMs as possessing the strongest antitumor effects, demonstrated by their correlation with effector $CD8^+$ T-cell signatures. Notably, chromatin accessibility suggests that both major subsets retain reprogramming potential toward this state. A recent study showed that a similar ISG phenotype can be induced in TAMs using a STING agonist (40). Myeloid-specific *Adar* deletion expanded ISG^+ TAMs, enhancing CXCL10–CXCR3 and CD40–CD40L interactions with $CD8^+$ T cells. Notably, $CXCL9/10^+$ TAMs have been reported to spatially co-localize with $IFN\gamma^+$ T cells, which may explain the mechanism by which ISG^+ TAMs promote antitumor responses (41). Together, these findings suggest that ISG^+ reprogramming via *Adar* inactivation could serve as a promising TAM-targeting strategy, holding great promise for the development of innovative immunotherapies.

Data Availability

The data and code used in this study are available from the following sources: The human pan-cancer single-cell transcriptional atlas of TAMs was obtained from publicly deposited data in the original article (7) and at http://panmyeloid.cancer-pku.cn. The human spatial transcriptomics data for the NSCLC were downloaded from the NanoString website (https://nanostring.com/products/cosmx-spatial-molecular-imager/ffpe-dataset/nsclc-ffpe-dataset/), and the data for colorectal cancer were downloaded from the 10x Genomics website (https://www.10xgenomics.com/products/visium-hd-spatial-gene-expression/dataset-human-crc). The human

scRNA-seq datasets were obtained from Gene Expression Omnibus (https://www.ncbi.nlm.nih.gov/geo/) and ArrayExpress (https://www.ebi.ac.uk/arrayexpress/). The accession numbers for these datasets are provided in Supplementary Table S7.

All data, including bulk RNA-seq, scRNA-seq, CROP-seq, and ATAC-seq data, that were generated in this study have been deposited in the NCBI Gene Expression Omnibus (GSE237788 and GSE269031). The spatial transcriptomics data and spatial metabolomics data that were generated in this study have been deposited at Zenodo (https://zenodo.org/records/16945965). All original code has been deposited at GitHub (https://github.com/zenglab-pku/TAM_paper).

The data and code will be publicly available as of the date of publication.

Authors' Disclosures

D. Pan reports grants from Bayer AG, Boehringer Ingelheim, and Sinopharm outside the submitted work. No disclosures were reported by the other authors.

Authors' Contributions

Y. Lu: Conceptualization, formal analysis, validation, investigation, methodology, writing–original draft. **C. Luo:** Conceptualization, formal analysis, validation, investigation, methodology, writing–original draft. **L. Huang:** Formal analysis, validation, investigation. **G. Wu:** Formal analysis, validation, investigation. **L. Zhong:** Formal analysis, validation, investigation. **J. Chu:** Formal analysis, validation, investigation. **F. Wang:** Resources, investigation. **Z. Zeng:** Conceptualization, formal analysis, supervision, funding acquisition, writing–review and editing. **D. Pan:** Conceptualization, formal analysis, supervision, funding acquisition, project administration, writing–review and editing.

Acknowledgments

We thank all the members of the Pan and Zeng labs for their comments and suggestions. This work was supported by National Natural Science Foundation of China grant (82341026 and 82073163; D. Pan), the National Key Research and Development Program of China No. 2022YFC2505400 (D. Pan), Tsinghua University Initiative Scientific Research Program (D. Pan), and the Tsinghua-Peking University Center for Life Sciences (D. Pan and Z. Zeng).

Note

Supplementary data for this article are available at Cancer Immunology Research Online (http://cancerimmunolres.aacrjournals.org/).

Received April 14, 2025; revised June 18, 2025; accepted August 27, 2025; posted first September 4, 2025.

References

1. Cassetta L, Pollard JW. Targeting macrophages: therapeutic approaches in cancer. Nat Rev Drug Discov 2018;17:887–904.
2. Robinson A, Han CZ, Glass CK, Pollard JW. Monocyte regulation in homeostasis and malignancy. Trends Immunol 2021;42:104–19.
3. Qian BZ, Pollard JW. Macrophage diversity enhances tumor progression and metastasis. Cell 2010;141:39–51.
4. Christofides A, Strauss L, Yeo A, Cao C, Charest A, Boussiotis VA. The complex role of tumor-infiltrating macrophages. Nat Immunol 2022;23:1148–56.
5. Mantovani A, Marchesi F, Jaillon S, Garlanda C, Allavena P. Tumor-associated myeloid cells: diversity and therapeutic targeting. Cell Mol Immunol 2021;18:566–78.
6. van Vlerken-Ysla L, Tyurina YY, Kagan VE, Gabrilovich DI. Functional states of myeloid cells in cancer. Cancer Cell 2023;41:490–504.
7. Cheng S, Li Z, Gao R, Xing B, Gao Y, Yang Y, et al. A pan-cancer single-cell transcriptional atlas of tumor infiltrating myeloid cells. Cell 2021;184:792–809.e23.
8. Zhang L, Li Z, Skrzypczynska KM, Fang Q, Zhang W, O'Brien SA, et al. Single-cell analyses inform mechanisms of myeloid-targeted therapies in colon cancer. Cell 2020;181:442–59.e29.
9. Dong L, Chen C, Zhang Y, Guo P, Wang Z, Li J, et al. The loss of RNA N^6-adenosine methyltransferase Mettl14 in tumor-associated macrophages promotes $CD8^+$ T cell dysfunction and tumor growth. Cancer Cell 2021;39:945–57.e10.
10. Mulder K, Patel AA, Kong WT, Piot C, Halitzki E, Dunsmore G, et al. Cross-tissue single-cell landscape of human monocytes and macrophages in health and disease. Immunity 2021;54:1883–900.e5.
11. Kloosterman DJ, Akkari L. Macrophages at the interface of the co-evolving cancer ecosystem. Cell 2023;186:1627–51.
12. Ma RY, Black A, Qian BZ. Macrophage diversity in cancer revisited in the era of single-cell omics. Trends Immunol 2022;43:546–63.
13. Li W, Xu H, Xiao T, Cong L, Love MI, Zhang F, et al. MAGeCK enables robust identification of essential genes from genome-scale CRISPR/Cas9 knockout screens. Genome Biol 2014;15:554.
14. Yang L, Wang J, Altreuter J, Jhaveri A, Wong CJ, Song L, et al. Tutorial: integrative computational analysis of bulk RNA-sequencing data to characterize tumor immunity using RIMA. Nat Protoc 2023;18:2404–14.
15. Wilkinson AC, Ishida R, Kikuchi M, Sudo K, Morita M, Crisostomo RV, et al. Long-term ex vivo haematopoietic-stem-cell expansion allows nonconditioned transplantation. Nature 2019;571:117–21.
16. Wilkinson AC, Ishida R, Nakauchi H, Yamazaki S. Long-term ex vivo expansion of mouse hematopoietic stem cells. Nat Protoc 2020;15:628–48.
17. Dura B, Choi JY, Zhang K, Damsky W, Thakral D, Bosenberg M, et al. scFTD-seq: freeze-thaw lysis based, portable approach toward highly distributed single-cell 3 mRNA profiling. Nucleic Acids Res 2019;47:e16.
18. Luo Z, He J, Chen Y, He J, Gong T, Tang F, et al. Air flow-assisted ionization imaging mass spectrometry method for easy whole-body molecular imaging under ambient conditions. Anal Chem 2013;85:2977–82.
19. He S, Bhatt R, Brown C, Brown EA, Buhr DL, Chantranuvatana K, et al. High-plex imaging of RNA and proteins at subcellular resolution in fixed tissue by spatial molecular imaging. Nat Biotechnol 2022;40:1794–806.
20. Bokhart MT, Nazari M, Garrard KP, Muddiman DC. MSiReader v1.0: evolving open-source mass spectrometry imaging software for targeted and untargeted analyses. J Am Soc Mass Spectrom 2018;29:8–16.
21. Wang G, Heijs B, Kostidis S, Mahfouz A, Rietjens RGJ, Bijkerk R, et al. Analyzing cell-type-specific dynamics of metabolism in kidney repair. Nat Metab 2022;4:1109–18.
22. Ashuach T, Gabitto MI, Koodli RV, Saldi GA, Jordan MI, Yosef N. MultiVI: deep generative model for the integration of multimodal data. Nat Methods 2023;20:1222–31.
23. Varrone M, Tavernari D, Santamaria-Martínez A, Walsh LA, Ciriello G. CellCharter reveals spatial cell niches associated with tissue remodeling and cell plasticity. Nat Genet 2024;56:74–84.
24. Miller BF, Bambah-Mukku D, Dulac C, Zhuang X, Fan J. Characterizing spatial gene expression heterogeneity in spatially resolved single-cell transcriptomic data with nonuniform cellular densities. Genome Res 2021;31:1843–55.
25. Cortese N, Carriero R, Barbagallo M, Putignano AR, Costa G, Giavazzi F, et al. High-resolution analysis of mononuclear phagocytes reveals GPNMB as a prognostic marker in human colorectal liver metastasis. Cancer Immunol Res 2023;11:405–20.
26. Pombo Antunes AR, Scheyltjens I, Lodi F, Messiaen J, Antoranz A, Duerinck J, et al. Single-cell profiling of myeloid cells in glioblastoma across species and disease stage reveals macrophage competition and specialization. Nat Neurosci 2021;24:595–610.
27. Katzenelenbogen Y, Sheban F, Yalin A, Yofe I, Svetlichnyy D, Jaitin DA, et al. Coupled scRNA-seq and intracellular protein activity reveal an immunosuppressive role of TREM2 in cancer. Cell 2020;182:872–85.e19.
28. Colegio OR, Chu NQ, Szabo AL, Chu T, Rhebergen AM, Jairam V, et al. Functional polarization of tumour-associated macrophages by tumour-derived lactic acid. Nature 2014;513:559–63.
29. Datlinger P, Rendeiro AF, Schmidl C, Krausgruber T, Traxler P, Klughammer J, et al. Pooled CRISPR screening with single-cell transcriptome readout. Nat Methods 2017;14:297–301.
30. Traag VA, Waltman L, van Eck NJ. From Louvain to Leiden: guaranteeing well-connected communities. Sci Rep 2019;9:5233.
31. Dougan M, Dranoff G, Dougan SK. GM-CSF, IL-3, and IL-5 family of cytokines: regulators of inflammation. Immunity 2019;50:796–811.
32. Certo M, Llibre A, Lee W, Mauro C. Understanding lactate sensing and signalling. Trends Endocrinol Metab 2022;33:722–35.

33. Jin K, Qian C, Lin J, Liu B. Cyclooxygenase-2-Prostaglandin E2 pathway: a key player in tumor-associated immune cells. Front Oncol 2023;13:1099811.
34. Lee DC, Sohn HA, Park ZY, Oh S, Kang YK, Lee KM, et al. A lactate-induced response to hypoxia. Cell 2015;161:595–609.
35. Efremova M, Vento-Tormo M, Teichmann SA, Vento-Tormo R. CellPhoneDB: inferring cell-cell communication from combined expression of multi-subunit ligand-receptor complexes. Nat Protoc 2020;15:1484–506.
36. Nalio Ramos R, Missolo-Koussou Y, Gerber-Ferder Y, Bromley CP, Bugatti M, Núñez NG, et al. Tissue-resident FOLR2^{+} macrophages associate with CD8^{+} T cell infiltration in human breast cancer. Cell 2022;185:1189–207.e25.
37. Su X, Xu Y, Fox GC, Xiang J, Kwakwa KA, Davis JL, et al. Breast cancer-derived GM-CSF regulates arginase 1 in myeloid cells to promote an immunosuppressive microenvironment. J Clin Invest 2021;131:e145296.
38. Wu JY, Huang TW, Hsieh YT, Wang YF, Yen CC, Lee GL, et al. Cancer-derived succinate promotes macrophage polarization and cancer metastasis via succinate receptor. Mol Cell 2020;77:213–27.e5.
39. Caronni N, La Terza F, Vittoria FM, Barbiera G, Mezzanzanica L, Cuzzola V, et al. IL-1β^{+} macrophages fuel pathogenic inflammation in pancreatic cancer. Nature 2023;623:415–22.
40. Wang Q, Bergholz JS, Ding L, Lin Z, Kabraji SK, Hughes ME, et al. STING agonism reprograms tumor-associated macrophages and overcomes resistance to PARP inhibition in BRCA1-deficient models of breast cancer. Nat Commun 2022;13:3022.
41. Bill R, Wirapati P, Messemaker M, Roh W, Zitti B, Duval F, et al. CXCL9: SPP1 macrophage polarity identifies a network of cellular programs that control human cancers. Science 2023;381:515–24.